

NIR Spectroscopy of Star-Forming Galaxies at $z \sim 1.4$ with Subaru/FMOS: The Mass–Metallicity Relation

Kiyoto YABE,^{1*} Kouji OHTA,¹ Fumihide IWAMURO,¹ Suraphong YUMA,¹ Masayuki AKIYAMA,²
 Naoyuki TAMURA,³ Masahiko KIMURA,³ Naruhisa TAKATO,³ Yuuki MORITANI,¹ Masanao SUMIYOSHI,¹
 Toshinori MAIHARA,¹ John SILVERMAN,⁴ Gavin DALTON,^{5,6} Ian LEWIS,⁵ David BONFIELD,^{5,7}
 Hanshin LEE,^{5,8} Emma CURTIS LAKE,^{5,9} Edward MACAULAY,⁵ and Fraser CLARKE⁵

¹Department of Astronomy, Kyoto University, Kitashirakawa-Oiwake-Cho, Sakyo-ku, Kyoto 606-8502

kiyoyabe@kusastro.kyoto-u.ac.jp, ohta@kusastro.kyoto-u.ac.jp

²Astronomical Institute, Tohoku University, Aoba-ku, Sendai 980-8578

³Subaru Telescope, National Astronomical Observatory of Japan, 650 North A'ohoku Place, Hilo, HI 96720, USA

⁴Institute for the Physics and Mathematics of the Universe, The University of Tokyo, Kashiwanoha, Kashiwa, Chiba 277-8583

⁵Department of Astrophysics, University of Oxford, Keble Road, Oxford OX1 3RH, UK

⁶STFC Rutherford Appleton Laboratory, Chilton, Didcot, Oxfordshire OX11 0QX, UK

⁷Centre for Astrophysics Research, Science and Technology Research Institute, University of Hertfordshire, Hatfield AL10 9AB, UK

⁸McDonald Observatory, University of Texas at Austin, 1 University Station C1402, Austin, TX 78712, USA

⁹Institute for Astronomy, University of Edinburgh, Royal Observatory, Edinburgh EH9 3HJ, UK

(Received 2011 November 2; accepted 2011 December 15)

Abstract

We present near-infrared spectroscopic observations of star-forming galaxies at $z \sim 1.4$ with FMOS on the Subaru Telescope. We observed K -band selected galaxies in the SXDS/UDS fields with $K \leq 23.9$ mag, $1.2 \leq z_{\text{ph}} \leq 1.6$, $M_* \geq 10^{9.5} M_\odot$, and expected $F(\text{H}\alpha) \geq 10^{-16} \text{ erg s}^{-1} \text{ cm}^{-2}$; 71 objects in the sample have significant detections of $\text{H}\alpha$. For these objects, excluding possible AGNs, identified from the BPT diagram, gas-phase metallicities were obtained from the $[\text{N II}]/\text{H}\alpha$ line ratio. The sample is split into three stellar-mass bins, and the spectra are stacked in each stellar-mass bin. The mass–metallicity relation obtained at $z \sim 1.4$ is located between those at $z \sim 0.8$ and $z \sim 2.2$. We constrain the intrinsic scatter to be ~ 0.1 dex, or larger in the mass–metallicity relation at $z \sim 1.4$; the scatter may be larger at higher redshifts. We found trends that the deviation from the mass–metallicity relation depends on the SFR (Star-formation rate) and the half light radius: Galaxies with higher SFR and larger half light radii show lower metallicities at a given stellar mass. One possible scenario for the trends is the infall of pristine gas accreted from IGM, or through merger events. Our data points show larger scatter than the fundamental metallicity relation (FMR) at $z \sim 0.1$, and the average metallicities slightly deviate from the FMR. The compilation of the mass–metallicity relations at $z \sim 3$ to $z \sim 0.1$ shows that they evolve smoothly from $z \sim 3$ to $z \sim 0$ without changing the shape so much, except for the massive part at $z \sim 0$.

Key words: galaxies: abundances — galaxies: evolution — galaxies: high-redshift

1. Introduction

The gas-phase metallicity (hereafter, metallicity) is a fundamental parameter for understanding the formation and evolution of galaxies, because it traces past star-formation activity; metals in gas are produced in stars formed and returned into the inter-stellar medium (ISM) of galaxies. The metallicity is also affected by the inflow and outflow of gas. Thus, by investigating the metallicity and its cosmological evolution, the star-formation history of galaxies together with the gas inflow and outflow can be constrained.

The presence of a correlation between the stellar mass and the metallicity (hereafter, mass–metallicity relation) in the local universe is well known. Tremonti et al. (2004) established the mass–metallicity relation at $z \sim 0.1$ with a large sample (~ 53000) of Sloan Digital Sky Survey (SDSS) galaxies.

Tracing the cosmological evolution of the mass–metallicity relation is indispensable to reveal how galaxies have been evolving. At $z \sim 1$, the mass–metallicity relations and downsizing-like evolution to $z \sim 0.1$ were found; the less evolution can be seen in the massive part (e.g., Savaglio et al. 2005; Zahid et al. 2011). However, the anti-downsizing-like evolution of the mass–metallicity relations were also presented at similar redshifts (Lamareille et al. 2009; Pérez-Montero et al. 2009). The mass–metallicity relations were obtained at $z \sim 2$ by using ~ 90 galaxies (Erb et al. 2006) and at $z \sim 3$ by ~ 20 galaxies (Maiolino et al. 2008; Mannucci et al. 2009); a smooth evolution of the mass–metallicity relation from $z \sim 3$ to $z \sim 0$ is suggested. However, at $z \sim 2$, higher metallicities at a given stellar mass have been reported (Hayashi et al. 2009; Yoshikawa et al. 2010; Onodera et al. 2010) than those found by Erb et al. (2006). The discrepancy at $z \sim 2$ may be partly due to the small size of their samples (10–20). Since the redshift of $z = 1\text{--}2$ is close to the peak epoch in the cosmic star-formation history,

* Present address: Division of Optical and Infrared Astronomy, National Astronomical Observatory of Japan, 2-21-1 Osawa, Mitaka, Tokyo 181-8588.

establishing the mass–metallicity relation at this redshift is very important.

Although the metallicity correlates well with stellar mass, there is a scatter in the relation. Its origin may provide a clue to understand the process of chemical enrichment, and may be related to how the mass–metallicity relation evolves. At $z \sim 0.1$, Tremonti et al. (2004) found that the mass–metallicity relation has an intrinsic scatter of ~ 0.1 , and the scatter is larger at a lower stellar mass. At a given stellar mass, galaxies with higher surface stellar mass density tends to show higher metallicity, suggesting that they transformed more gas into stars while raising the metallicity. Ellison et al. (2008a) showed that galaxies with a larger specific star-formation rate (*SFR*) and size show lower metallicity at a given stellar mass at $z \sim 0.1$. More recently, Mannucci et al. (2010) and Yates, Kauffmann, and Guo (2012) found that galaxies with larger *SFRs* tend to show lower metallicities at $z \sim 0.1$, and that the scatter around the mass–metallicity relation is greatly reduced (i.e., the fundamental metallicity relation) by introducing *SFR* as the second parameter affecting the metallicity. The scatter of the mass–metallicity relation, however, is still unclear at higher redshifts because of the limited sample size. In order to investigate these trends further, including the dependency of other parameters, at higher redshift, a large near-infrared spectroscopic survey is necessary, which is very time consuming and hard to achieve.

The Fiber Multi Object Spectrograph (FMOS) on the Subaru Telescope enables us to survey a large spectroscopic sample at high redshifts. FMOS is a near infrared (NIR) fiber multi-spectrograph (Kimura et al. 2010). The fiber positioner “Echidna” at the prime focus feeds 400 fibers in a FoV of 30' diameter. Two NIR spectrographs (IRS 1 and IRS 2) with an OH airglow suppression system are capable of obtaining both low-resolution ($R \sim 650$) and high-resolution ($R \sim 3000$) spectra in the wavelength range of 0.9–1.8 μm . Taking advantage of the multiplicity available with FMOS, we are conducting a large spectroscopic survey for star-forming galaxies at $z = 1$ –2. This redshift range is of much interest, because it is near, or shortly after, the peak epoch in the cosmic star-formation history (e.g., Hopkins & Beacom 2006), and is thus important for the history of the chemical evolution of galaxies. It is also suitable for FMOS, because in the redshift range [N II] $\lambda\lambda$ 6548, 6584, H α , [O III] $\lambda\lambda$ 4959, 5007, and H β lines are located in the wavelength range observable with FMOS. In this paper we present the first results from this survey regarding metallicity measurements of galaxies at $z \sim 1.4$.

Throughout this paper, we adopt concordance cosmology, $(\Omega_M, \Omega_\Lambda, h) = (0.3, 0.7, 0.7)$. All magnitudes are in the AB system (Oke & Gunn 1983).

2. Sample and Observations

2.1. Photometric Data in the SXDS/UDS Fields

The sample is selected from a galaxy catalog in the SXDS/UDS fields, where deep multi-wavelength data are available. The optical Subaru/Suprime-Cam images (B , V , R_C , i' , and z') are available from the Subaru-XMM Deep Survey (SXDS: Furusawa et al. 2008) with the original pixel scale of $0''.202 \text{ pixel}^{-1}$. The limiting magnitudes are 27.7,

27.2, 27.1, 27.0, and 26.0 mag for B , V , R_C , i' , and z' -band, respectively (5σ , $2''.0$ diameter). The NIR UKIRT/WFCAM images (J , H , and K_s) are taken from the DR8 version of the UKIDSS Ultra Deep Survey (UDS: Lawrence et al. 2007) with the original pixel scale of $0''.268 \text{ pixel}^{-1}$. The limiting magnitudes are 24.9, 24.2, and 24.6 mag for J , H , and K_s , respectively (5σ , $2''.0$ diameter). The Spitzer/IRAC images (3.6 μm , 4.5 μm , 5.8 μm , and 8.0 μm) are taken from the Spitzer public legacy survey of the UKIDSS Ultra Deep Survey (SpUDS; PI: J. Dunlop in preparation) with the original pixel scale of $0''.600 \text{ pixel}^{-1}$. The limiting magnitudes are 24.8, 24.5, 22.8, and 22.7 mag for ch1 (3.6 μm), ch2 (4.5 μm), ch3 (5.8 μm), ch4 (8.0 μm), respectively (5σ , $2''.4$ diameter). We use an overlapped area of these data. The effective area is $\sim 0.67 \text{ deg}^2$.

The NIR and MIR images are aligned to the optical images with a pixel scale of $0''.202 \text{ pixel}^{-1}$. Object detection and photometry in each image is carried out with respect to a reference K_s -band image by using the *double image* mode of SExtractor (Bertin & Arnouts 1996). For the optical and NIR images, aperture photometry with an aperture of $2''.0$ diameter is carried out after applying PSF matching. The total magnitude is calculated from the aperture magnitude scaled to the SExtractor’s MAG_AUTO in the K_s -band. For IRAC images, the total magnitude is calculated from the aperture magnitude with $2''.4$ diameter by applying aperture corrections. The correction factors are determined by generating artificial objects with various intrinsic sizes on the IRAC images, and recovering the aperture magnitudes. The uncertainties of the aperture correction in the above simulations are 0.05, 0.05, 0.09, and 0.08 mag for ch1, ch2, ch3, and ch4, respectively.

2.2. Photometric Redshift Sample

For each source, the photometric redshift (photo- z) is determined by using Hyperz (Bolzonella et al. 2000), where model templates are fitted to the observed Spectral Energy Distributions (SEDs) from optical to MIR by a standard χ^2 minimization. We use a standard set of synthetic spectra with 51 age grids from 0.3 Myr to 20 Gyr and 21 reddening (A_V) grids from 0.0 to 4.0 with $\Delta A_V = 0.2 \text{ mag}$. We also use the CWW (Coleman et al. 1980) templates. The range of the photo- z is set to be $0.0 < z_{\text{ph}} < 6.0$ with a step of $\Delta z = 0.03$. The obtained photo- z is compared with the available spectroscopic redshift (spec- z) in the SXDS/UDS (C. Simpson et al. in preparation; M. Akiyama et al. in preparation; Smail et al. 2008). Although some catastrophic outliers exist, the photo- z generally agrees with the spec- z with an uncertainty of $\sigma_z/(1+z) = 0.02$ – 0.03 at $z = 1$ –2.

In order to derive stellar masses of these galaxies, we performed a SED fitting by using the SEDfit (Sawicki 2011). For model SEDs, we used the BC03 population synthesis code (Bruzual & Charlot 2003) with Padova 1994 evolutionary tracks. The Salpeter IMF (Salpeter 1955) with a mass range of 0.1–100 M_\odot and a metallicity of 1.0 Z_\odot are assumed. The extinction curve of Calzetti et al. (2000) is also assumed. We fix redshifts to those determined by the Hyperz in order to reduce the number of free parameters. We generate model SEDs with 25 age grids from 0.2 Myr to 15.8 Gyr, 5 star-formation histories (constant SF, $\tau = 1 \text{ Gyr}$, $\tau = 100 \text{ Myr}$, $\tau = 10 \text{ Myr}$, and instantaneous burst grids, and 21 $E(B - V)$

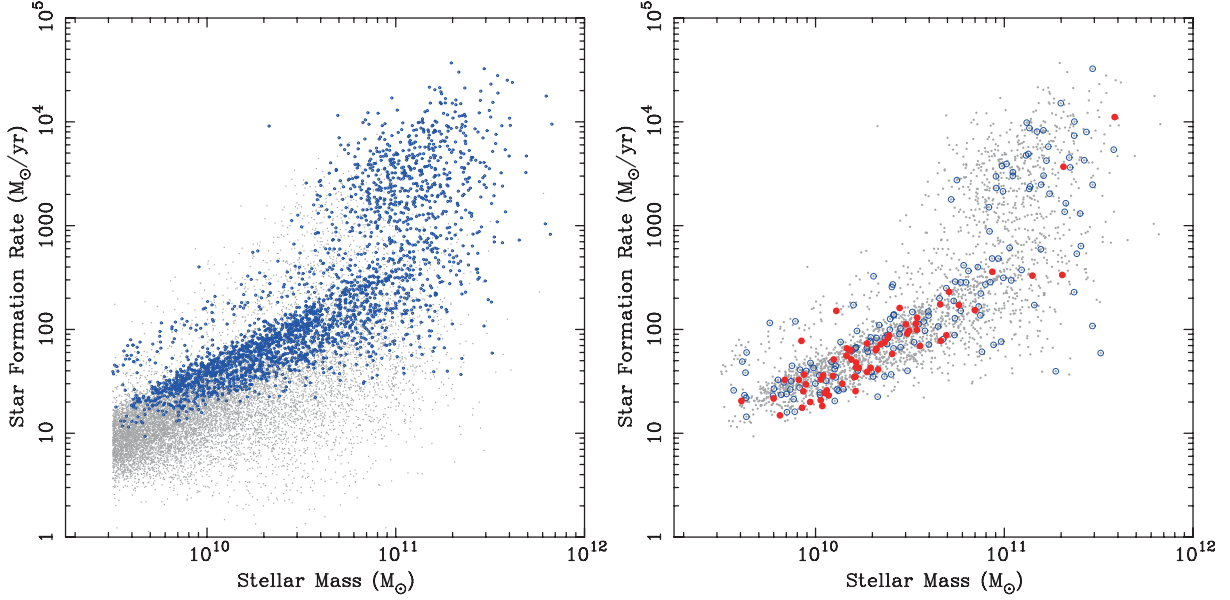


Fig. 1. Our targets on the M_* – SFR diagram. Left: Our primary sample with $K_s < 23.9$ mag, $1.2 \leq z_{\text{ph}} \leq 1.6$, and $M_* \geq 10^{9.5} M_\odot$ is indicated by gray dots. Among the primary sample, the secondary sample with expected $F(\text{H}\alpha) \geq 1 \times 10^{-16} \text{ erg s}^{-1} \text{ cm}^{-2}$ is indicated by blue open circles. Right: Objects observed with FMOS are plotted as circles. While objects whose $\text{H}\alpha$ lines are detected with S/N of > 3 are indicated by red filled circles, objects whose $\text{H}\alpha$ is not detected with S/N of > 3 are indicated by blue open circles. The secondary sample are also plotted by gray dots.

grids from 0.0 to 1.0 with a step of $\Delta E(B - V) = 0.05$ mag. We then fit the model SEDs to the observed SEDs with the standard χ^2 minimization.

The color excesses are estimated from the rest-frame UV colors. It is known that the rest-frame UV color strongly correlates with $E(B - V)$ (Meurer et al. 1999). For objects at $z \sim 2$, Daddi et al. (2004, 2007) presented the relation between $B - z'$ color and $E(B - V)$ by calibrating with the results from the SED fitting. For the redshift range of our sample, the $B - z'$ color is not a good indicator of extinction, because the z' -band covers beyond the Balmer/4000 Å break. For $1.2 < z < 1.6$, we calibrate the relation between the $B - i'$ color and $E(B - V)$ by using the results of the SED fitting. The resulting relation is $E(B - V) = 0.31(B - i') + 0.02$. All of the color excess of our sample is derived from the $B - i'$ color by using this relation. As we mention in section 3, both $\text{H}\alpha$ and $\text{H}\beta$ lines are detected in some galaxies. For these objects, the color excess can be derived based on the Balmer decrement, by assuming an intrinsic $\text{H}\alpha/\text{H}\beta$ ratio of 2.86 and the Calzetti extinction law. The average result is consistent with the color excess from the rest-frame UV colors within the error, if the extinction for the nebular emission is assumed to be larger than that for the stellar continuum, as we describe below.

The SFR is derived from the rest-frame UV luminosity density by using a conversion by Kennicutt (1998). The rest-frame UV luminosity density is calculated from the B -band magnitude. The intrinsic SFR is derived by correcting for the extinction with the $E(B - V)$ derived above. The Calzetti extinction curve is also assumed. For some objects, we cross-check with the SFR s from MIPS fluxes by using archived images of the SpUDS. We use the conversion from the rest-frame $L_{8\mu\text{m}}$ to the SFR by Daddi et al. (2007). The resulting SFR from IR luminosity roughly agrees with that

from the rest-frame UV luminosity density.

The expected $\text{H}\alpha$ flux is calculated from the intrinsic SFR and the $E(B - V)$ described above. Since it is suggested that the extinction is significantly larger for the ionized gas than for the stellar component (Calzetti et al. 2000), we convert the obtained $E(B - V)$ to that for the ionized gas by using a prescription by Cid Fernandes et al. (2005). For conversion from the SFR to the $\text{H}\alpha$ luminosity, we use the relation by Kennicutt (1998).

The sample is cross-correlated with X-ray sources (Ueda et al. 2008), and objects which are cross-matched within the error circle of the X-ray source are excluded from the sample. Accordingly, the X-ray bright AGNs ($L_{\text{X}(2-10\text{keV})} \gtrsim 10^{43} \text{ erg s}^{-1}$) are excluded from our sample.

2.3. Sample

For spectroscopic observations with FMOS, the primary sample is constructed from the K -selected catalogue described above with the following selection criteria: $K_s < 23.9$ mag, $1.2 \leq z_{\text{ph}} \leq 1.6$, and $M_* \geq 10^{9.5} M_\odot$. This primary sample size is very large, and many of the sample galaxies may show very faint $\text{H}\alpha$ emission lines. Thus, in order to make an efficient survey, and as a first step, we selected objects for which the expected $\text{H}\alpha$ flux is larger than $1.0 \times 10^{-16} \text{ erg s}^{-1} \text{ cm}^{-2}$ as the secondary sample. This selection could introduce some bias for the sample, and hence the effects will be considered later based on the obtained results.

In figure 1, intrinsic SFR s derived from the rest-frame UV are plotted against the stellar mass (hereafter M_* – SFR diagram) for the primary sample. The SFR correlates with the stellar mass. On the M_* – SFR diagram, the secondary sample is also shown with blue open circles. The distribution is slightly shifted toward larger SFR at a given stellar mass,

particularly in a less-massive part. This is due to the fact that we selected objects with a larger expected $H\alpha$ flux, and thus a larger intrinsic SFR . We discuss the effect of the selection bias on the metallicity in subsection 3.9. Actually, the observed objects were randomly selected from the secondary sample. The right panel of figure 1 shows the observed objects among the secondary sample.

Some target objects are relatively massive ($M_* \gtrsim 5 \times 10^{10} M_\odot$), and have a high intrinsic SFR ($\gtrsim 1000 M_\odot \text{yr}^{-1}$), as can be seen in figure 1. We cross-correlated to the MIPS sources, and found that the detection rate in MIPS is significantly lower for these objects than for other objects. The estimation of these high SFR s may be incorrect, partly because the $E(B - V)$ is overestimated due to the dust/age degeneracy. We included these objects in our targeted sample, and found that the actual detection rate of $H\alpha$ emission for the galaxies in this M_* - SFR region is significantly lower than that in the other region, as can be seen in the right panel of figure 1.

2.4. Observations and Data Reduction

The observations were carried out with FMOS (Kimura et al. 2010) on the Subaru Telescope on 2010 September 27–28, November 11–13, 21–24, 28, and December 15–16, (mostly the guaranteed time observing runs and partly an engineering observing run for science verification, and open-use observations). The observations were made with the Cross Beam Switch (CBS) mode in the low-resolution (LR) mode employing both IRS 1 and IRS 2. The spectral resolution in the LR mode was $R \sim 500$ at $\lambda \sim 1.10 \mu\text{m}$, $R \sim 650$ at $\lambda \sim 1.30 \mu\text{m}$, and $R \sim 800$ at $\lambda \sim 1.55 \mu\text{m}$, which were measured from the Th-Ar lamp frames. The pixel scale in the LR-mode was 5 \AA . Our targets were allocated to fibers together with other scientific targets. Although the weather conditions varied during the observing runs, the typical exposure time was $\sim 3 \text{ hr}$ for one FMOS field of view. The typical seeing size measured with the FMOS sky-camera during the observations was $0''.9$ in the R -band.

The obtained data were reduced with the FMOS pipeline FIBRE-pac and detailed descriptions for the data reduction are presented by Iwamuro et al. (2012). Here, we describe an outline of the process. For a set of exposures, $A - B$ sky subtraction was carried out. Then, the obtained 2D spectra were corrected for distortion, and residual sky subtraction was also carried out. The obtained spectra were combined for the total exposures. Since the spectrum of one target was obtained by two fibers in the CBS mode, the final spectrum of one target was obtained by merging the CBS pair spectra. Wavelength calibration was done by using Th-Ar lamp frames. The uncertainty associated with the wavelength calibration was $\Delta\lambda \sim 5 \text{ \AA}$. The relative flux calibration was done by using several F, G, or K-type stars, selected based on the $J - H$ and $H - K_s$ colors and the observed simultaneously with other scientific targets. The uncertainty of the relative flux calibration was $\sim 10\%$ at $\lambda = 1.0\text{--}1.8 \mu\text{m}$. The absolute flux was determined from the observed count rate by assuming the total throughput of the instrument, which was calibrated by using moderately bright stars ($\sim 16 \text{ mag}$ in J - or H -band) under the best weather conditions ($\sim 0''.7$) in previous engineering observations. The uncertainty of the absolute flux calibration, itself,

was estimated to be $\sim 10\%$. However, there may be additional uncertainties (20%–30%) that come from a variation of the atmospheric transmission and the seeing conditions.

In total, 317 objects were observed and for 71 objects the $H\alpha$ emission line was detected with a signal-to-noise ratio (S/N) larger than 3, where the noise level was measured from the continuum in a wavelength window of $\pm 0.1 \mu\text{m}$ from the emission line. The detection rates were 26%, 44%, 21%, and 9% at $M_* < 10^{10} M_\odot$, $10^{10} M_\odot \leq M_* < 10^{10.5} M_\odot$, $10^{10.5} M_\odot \leq M_* < 10^{11} M_\odot$, and $M_* \geq 10^{11} M_\odot$, respectively. Examples of the obtained spectra are presented in figure 2. Spectra in which the S/N of $[\text{N II}]\lambda 6584$ is larger than 3.0, $1.5 \leq S/N < 3.0$, $S/N < 1.5$ are shown in the left, middle, and right panels of the figure, respectively.

3. Results

3.1. Model Fitting to Emission Lines

In order to measure a spec- z , a flux of an emission line, and a line width, we made a model fit to the reduced one-dimensional emission line profile. This process is straightforward in the usual spectroscopy. In our case, however, we need rather complicated processes. FMOS uses an OH suppression system to remove the strong OH airglow sky emission lines. The dispersed light is focused onto a mask mirror with a resolving power of $R \sim 3000$ ($\sim 100 \text{ km s}^{-1}$), and is rejected by the OH masks. Then, the spectrum is anti-dispersed by a VPH grating to $R \sim 650$ ($\sim 450 \text{ km s}^{-1}$), and focused onto the detector [see Kimura et al. (2010) for the optical design of FMOS]. Since the reduced spectra are divided by a spectrum of the calibration star in the relative flux calibration process of the pipeline, the effect of the OH-mask on the continuum light is corrected in the final reduced spectra. The correction, however, is not appropriate for emission lines if the line width is relatively small. Thus, we present two different ways of spectral fitting. One is fitting with model spectra while taking into account the mask effects; the other is fitting the observed spectra without taking the mask effects into consideration. In both cases, we subtracted the continuum by fitting with third-order polynomials in the wavelength range of $1.45\text{--}1.70 \mu\text{m}$.

In the former method (*method1*), we fit model spectra including the OH-mask effect to the observed spectra. The model spectra are generated as follows. An intrinsic spectrum is modeled by a multi-Gaussian function with $H\alpha$ and $[\text{N II}]\lambda\lambda 6548, 6584$ lines. We assume that ratio of $[\text{N II}]\lambda 6584$ and $[\text{N II}]\lambda 6548$ is 3.0, the line widths are the same as that of $H\alpha$, and there is no systematic shift between the $H\alpha$ line and the $[\text{N II}]$ lines. Each spectrum is parametrized by four parameters: redshift, amplitude of $H\alpha$, amplitude of $[\text{N II}]\lambda 6584$, and line width. The spectrum represented by these parameters is convolved to a resolution of $R \sim 3400$, and then the flux density in the regions ($\Delta\lambda \sim 8 \text{ \AA}$) of the OH-masks is set to be zero. The obtained spectrum is convolved to a low-resolution spectrum with $R \sim 800$.

In order to correct the continuum level affected by OH-suppression, a flat spectrum in F_ν without emission lines mimicking a star used in the flux calibration is processed in the same manner as described above. The correction factors as a function of the wavelength are derived from the resulting

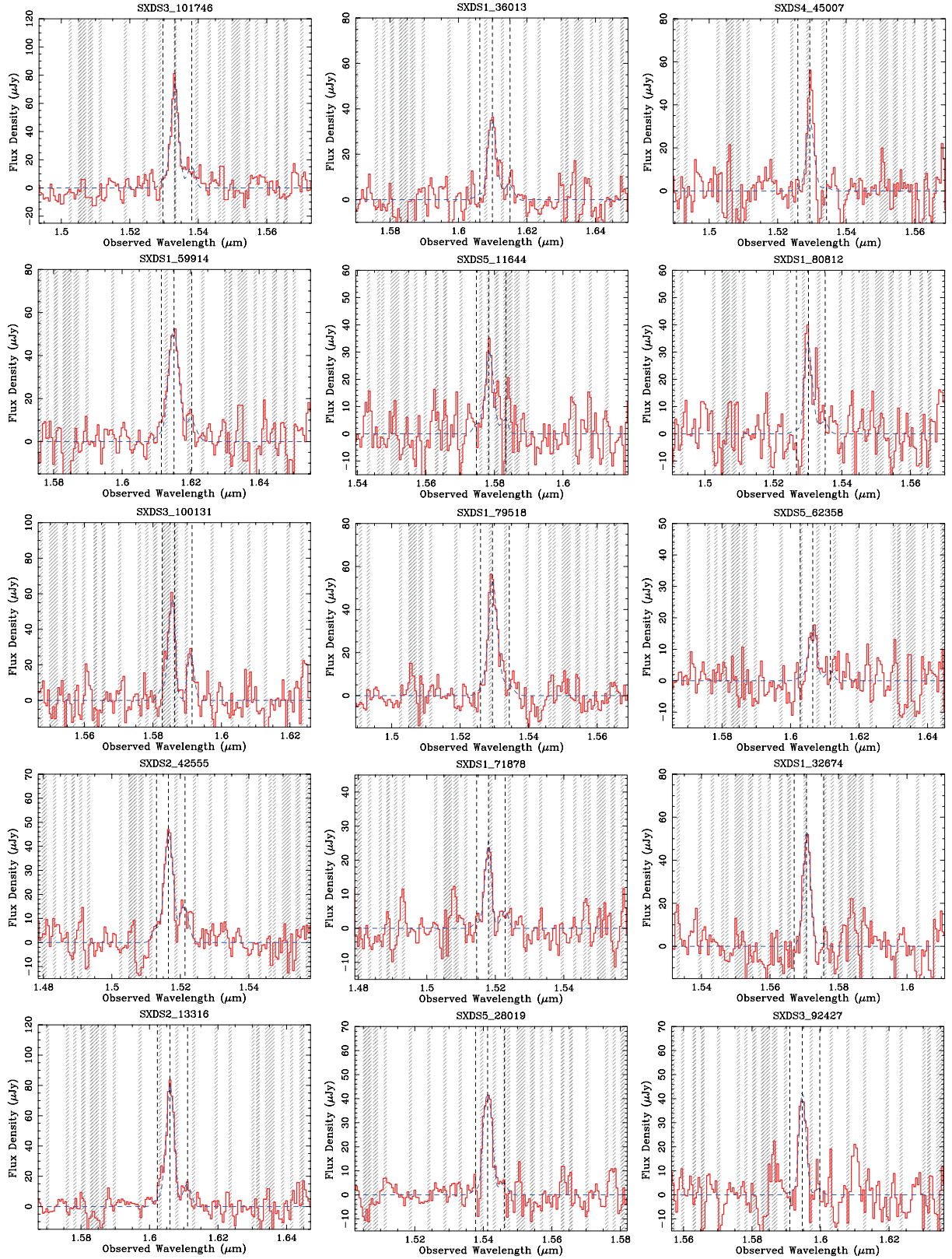


Fig. 2. Examples of the observed spectra (red solid lines) with the best-fitted models (blue dotted lines). In the left 5 panels, objects whose S/N s of $[\text{N II}]\lambda 6584$ lines are larger than 3 are plotted. In the middle panels, objects with $1.5 \leq S/N < 3.0$, and in the right panels, objects with $S/N < 1.5$ are plotted. Vertical dotted lines indicate the positions of $[\text{N II}]\lambda 6584$, $\text{H}\alpha$, and $[\text{N II}]\lambda 6584$, from left to right. The positions and the width of the OH-mask are indicated by hatched stripes. Continua were subtracted by third-order polynomial fitting.

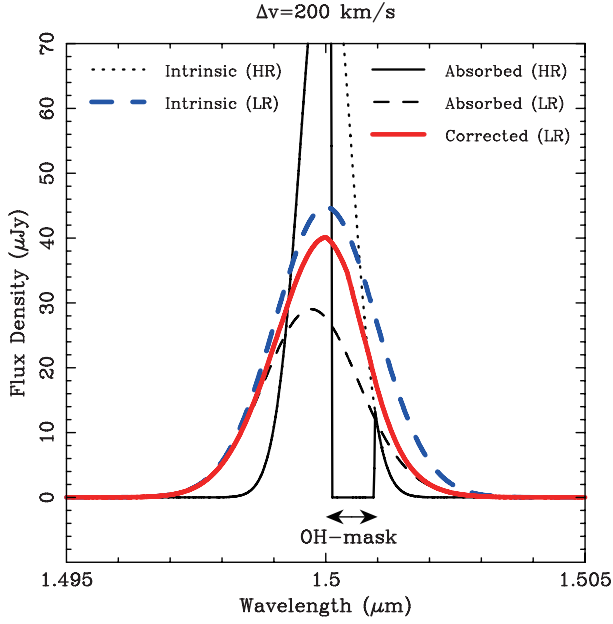


Fig. 3. Schematic view of the OH-mask effects. The intrinsic spectrum with Δv of 200 km s^{-1} in the HR mode and that absorbed by the OH-mask are indicated by a dotted line and a thin solid line, respectively. The absorbed spectrum degraded to the LR is indicated by a thin dashed line. The spectrum corrected for the mask effects by using continuum light is indicated by a thick solid line; this is the obtained spectrum after data reduction. The intrinsic spectrum degraded to the LR without considering the mask effect is shown by a thick dashed line as a reference. See also text for details.

spectrum divided by the input flat spectrum. The model spectrum with emission lines is corrected by using this correction factor in order to compare with the observed spectrum. A schematic view of line profiles affected by the OH-mask is presented in figure 3.

The fitting process is carried out using the *mpfit* package (Markwardt 2009), which implements a non-linear least-squares fitting with the standard Levenberg-Marquardt algorithm. In the fitting procedure, we search for the minimum χ^2 in the parameter space of the four parameters described above. The resulting χ^2 maps of fits show that there are no pronounced discontinuities or strong degeneracies between the parameters.

For the latter method (*method2*), we simply fit the observed spectrum by the multi-Gaussian profile. The fitting procedure is generally the same as *method1*. The fitting models are multi-Gaussian functions, but without taking the mask-loss corrections into consideration.

In order to quantify the effects of the OH-masks and to evaluate the accuracy of the two methods, we generate artificial spectra with one emission line and no continuum, while varying the line widths ($50\text{--}1000 \text{ km s}^{-1}$) and fluxes ($1.0 \times 10^{-17} - 1.0 \times 10^{-15} \text{ erg s}^{-1} \text{ cm}^{-2}$), which cover the ranges of widths and fluxes of most of the emission lines detected with $S/N \geq 1.5$. We then placed an OH-mask, virtually changing its wavelength randomly to simulate the amount of flux loss for an emission line at different redshifts. The final LR spectrum was then made by degrading the spectral resolution down to $R \sim 650$. The random noise, which is equivalent to the average noise level actually observed in a typical exposure time, was

added into each spectrum. The resulting artificial spectra were fitted by two different methods (*method1* and *method2*), and the obtained redshifts (wavelengths), line fluxes, and line widths were compared to the input values. We repeated this process 1000 times. The redshifts were recovered with an accuracy of $\lesssim 5\%$ in both methods. The line widths were underestimated by up to $\sim 50\%$ in *method2*. However, in *method1*, the line widths could be recovered properly with an accuracy of $\lesssim 20\%$.

The recovery rate of the flux against the amount of the loss by the mask is presented in figure 4. Our simulations show that *method2* cannot properly recover the flux, which is affected by the OH-mask, especially when the line width is small. For a line width of $\sim 50 \text{ km s}^{-1}$, up to $\sim 90\%$ of the line flux is damped by the OH-mask. In this case, the flux recovered by *method2* is only $\sim 20\%$ of the intrinsic flux, and $\sim 80\%$ of the light is lost. The recovery of the flux improves if the line width is larger. For instance, the flux can be recovered within $\lesssim 20\%$ accuracy if the line width is $\gtrsim 600 \text{ km s}^{-1}$. It is also interesting to note that the flux is overestimated by *method2* in some cases, because the line profile is overcorrected by the correction for the continuum. If a large part a pixel covers an OH-mask, and the peak of a narrow emission line just outside of the mask, the flux loss rate in the pixel for the continuum is larger than that for the emission line.

Figure 4 shows that the fluxes recovered by *method1* agree well with the intrinsic fluxes for any line width. The uncertainty of the correction is $\lesssim 20\%$ in most cases. If the loss is $\gtrsim 90\%$, however, the uncertainty is $\gtrsim 30\%$. Of course, the results are obtained from the simulations, and the actual uncertainty could be larger than these estimates. We exclude objects from the observed sample if the loss is calculated to be larger than 90% in the profile fitting. In this paper, we use *method1* as a fiducial line-fitting method.

3.2. Spec-z and H α Line Flux

The best-fit redshifts, which are referred to as spec-zs, are distributed from $1.2 \leq z \leq 1.6$ with a median of $z = 1.408$. In the upper left panel of figure 5, spec-z is compared to photo-z. Although spec-z generally agrees with photo-z with $\sigma \sim 0.05$, consistent with the uncertainty of the photo-z determination described in subsection 2.2, there appears to be a systematic difference of ~ 0.05 at $1.2 \leq z \leq 1.6$. This may be caused by the systematic uncertainty of the photometric zero-points. The presence of such systematic differences at some redshifts has also been reported by Ilbert et al. (2006).

In figure 5, we compare the fluxes of H α and [N II] emission lines obtained by two different methods. Although the flux derived from the two methods generally agree well for both emission lines, in some cases that measured by *method2* is underestimated significantly, which is consistent with the results of the simulations, indicating the necessity of corrections for the OH mask effects.

Comparisons of the observed H α flux and the expected H α flux are shown in figure 6. The observed H α fluxes were corrected for the fiber loss, depending on their r_{50} , as we describe in subsection 3.3. In the left panel, the expected H α fluxes calculated from the rest-frame UV luminosity, corrected for the nebular emission line using $E(B - V)$, agree well with the observed H α fluxes. In contrast, in the right panel,

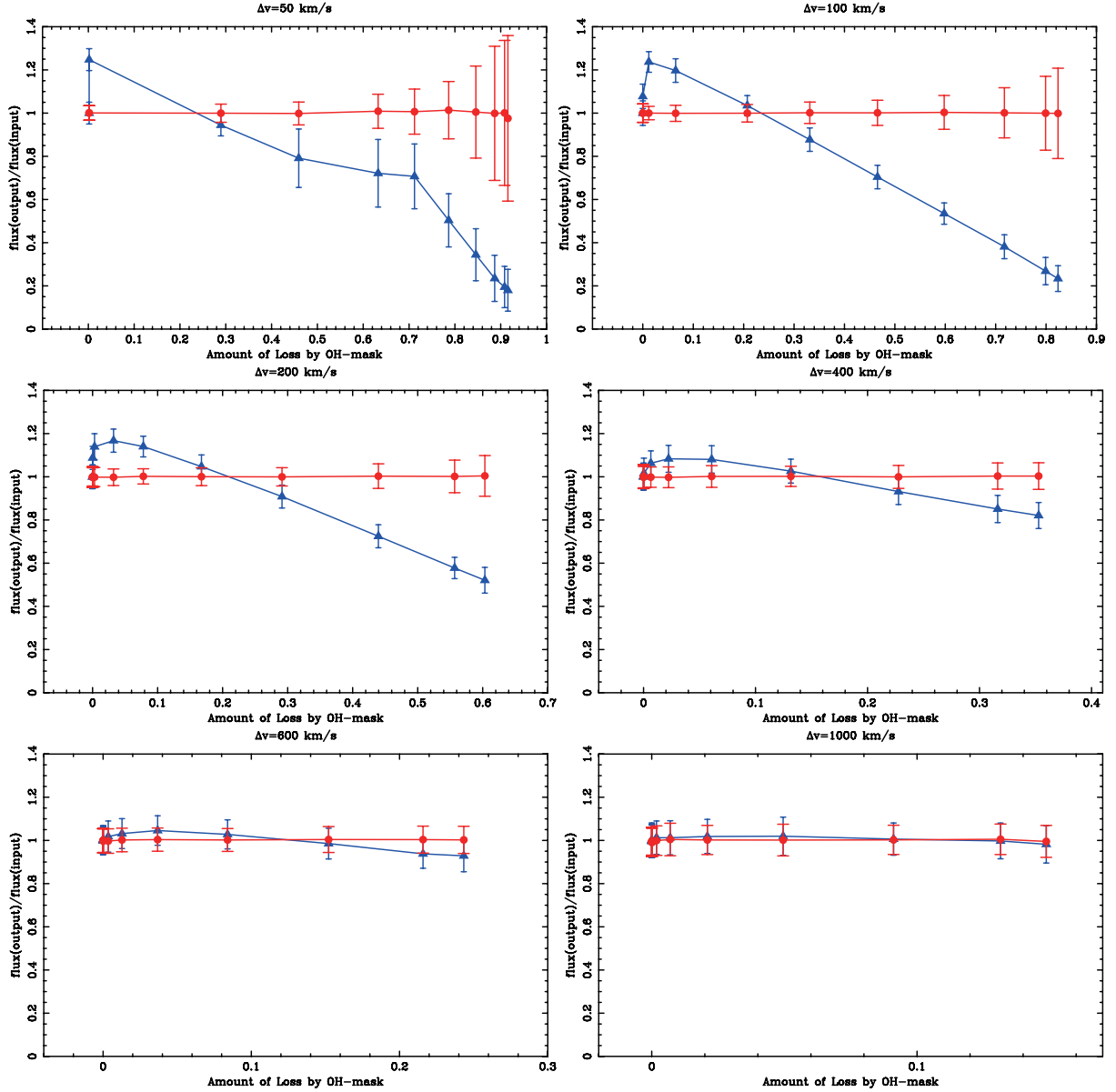


Fig. 4. Average ratio of recovered flux and the input flux against the amount of the loss by the OH-mask for intrinsic line widths of 50 km s^{-1} (top left), 100 km s^{-1} (top right), 200 km s^{-1} (middle left), 400 km s^{-1} (middle right), 600 km s^{-1} (bottom left), 1000 km s^{-1} (bottom right). Red lines and circles are the results by *method1*, while the blue lines and triangles are those by *method2*. Error bars indicate 1σ standard deviations of the simulated distributions. See text for details of the simulations.

the expected fluxes by assuming the $E(B - V)$ for the stellar component are systematically larger than the observed ones, implying that the dust extinction for the nebular emission is larger than that for the stellar continuum. Figure 7 shows that the SFR derived from the observed $H\alpha$ flux (extinction corrected for nebular component) agrees with that from the rest-frame UV luminosity density (extinction corrected for stellar component).

Since the $H\alpha$ emission line is superposed on the stellar absorption line, a correction for this effect is necessary in order to measure an accurate emission-line flux. Zahid, Kewley, and Bresolin (2011) fitted the stellar continuum of stacked spectra, and found that the correction to $H\beta$ emission is negligible in

galaxies at $z \sim 0.8$. Since the continua of our sample are mostly too weak to be fitted, we estimated the absorption contribution from the SED models as follows. We calculated the equivalent width (EW) of the $H\alpha$ absorption line by assuming an exponentially decaying star-formation history with $\tau = 10 \text{ Myr}$ and a stellar age of $\sim 100 \text{ Myr}$; a typical case in our SED fitting for the observed sample. The resulting EW of -4.2 \AA is much smaller ($\sim 2\%$) than the typical $H\alpha$ EW of $\sim 200 \text{ \AA}$, and thus we do not take the effect of stellar absorption into consideration.

3.3. Aperture Effect

A certain fraction of light outside the aperture of the FMOS

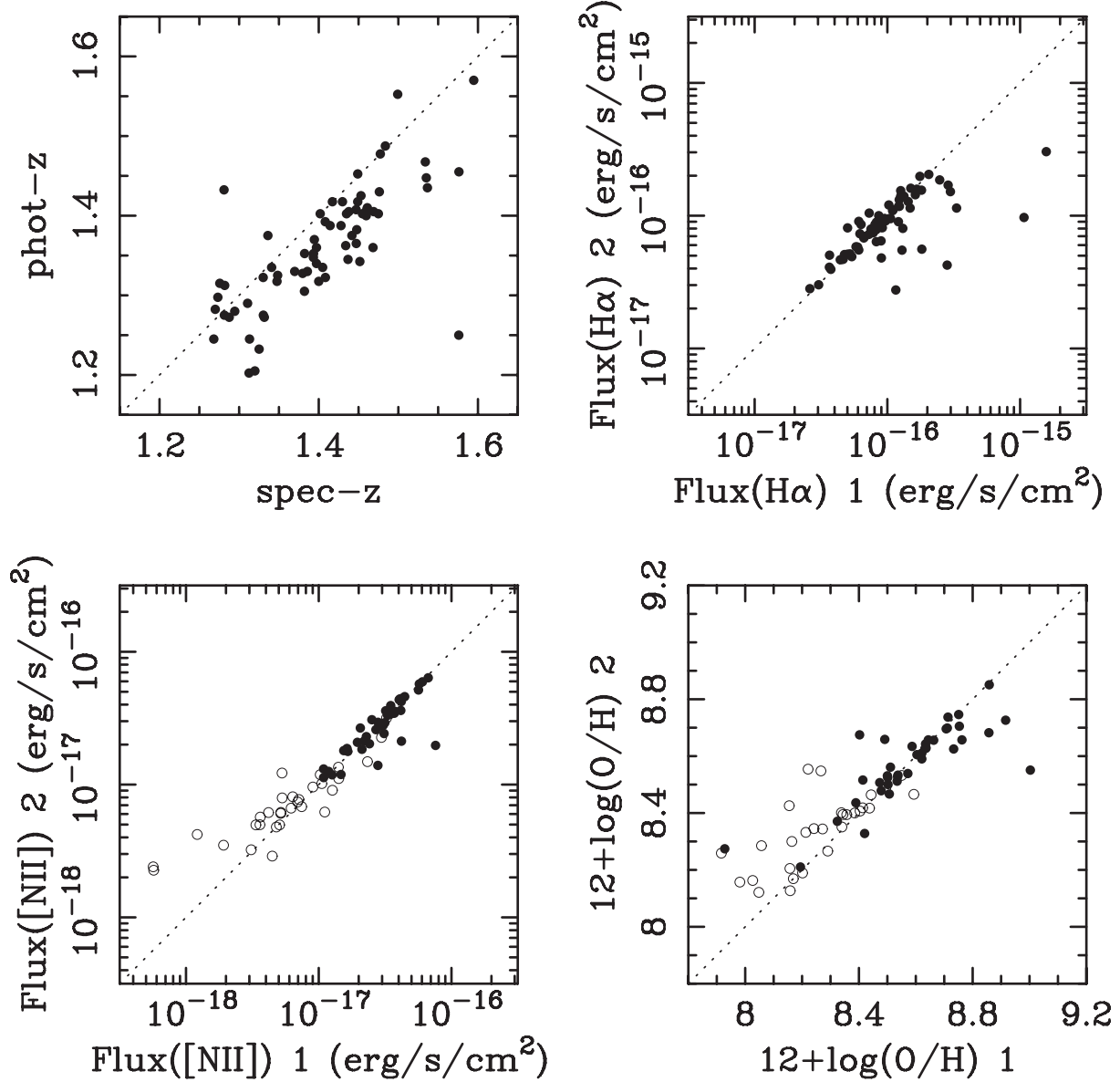


Fig. 5. Comparison between spec-z and photo-z (upper left). Comparisons of the H α flux (upper right), [N II] flux (lower left), and oxygen abundance (lower right) in two different spectral fitting methods. Open circles are objects whose S/N of [N II] flux is less than 1.5.

fiber of $1''/2$ diameter is lost. Although the aperture effect on the relative quantities, such as a line ratio and the metallicity is small, the effect is critical to absolute quantities, such as the total flux and *SFR*. We estimate the covering fraction for galaxies by using the NICMOS F160W archival images (Bouwens et al. 2010) convolved to the typical seeing sizes ($0''.5$, $0''.75$, $1''.00$, and $1''.20$ in FWHM) in the GOODS-N field. Object detection and $1''/2$ aperture photometry were carried out by using *SExtractor*. These objects were cross-matched with a *K*-selected catalogue in GOODS-N/MODS (Kajisawa et al. 2011; Yuma et al. 2011). For objects brighter than $K_s = 23.9$ mag and more massive than $M_* = 10^{9.5} M_\odot$ at $1.2 \leq z_{\text{ph}} \leq 1.6$, we calculated the covering fraction, which is defined as FLUX_APER (in $1''/2$ diameter) / FLUX_AUTO. The covering fraction correlates very well with a half light

radius deconvolved by the PSF (r_{50}) in the F160W image; the scatter is very small ($\lesssim 4\%$). According to simulations, the covering fractions are 0.20–0.80, depending on the seeing size; a typical value is ~ 0.5 when the seeing size is $0''.75$.

In order to estimate fiber aperture losses for our sample galaxies in the SXDS field, we firstly derived the observed r_{50} based on *K*-band WFCAM images by using the *SExtractor*'s FLUX_RADIUS. The intrinsic r_{50} of our sample was calculated from the observed r_{50} from the *K*-band image, after deconvolution by a Gaussian PSF of $0''.80$. The resulting r_{50} distributes from $0''.3$ to $0''.9$ with a median value of $0''.55$ (4.6 kpc at $z = 1.4$). In order to examine the reliability of the estimation in the *K*-band, these were compared to those obtained from higher-resolution images from WFC3/HST in the CANDELS survey held in a small part of the SXDS/UDS

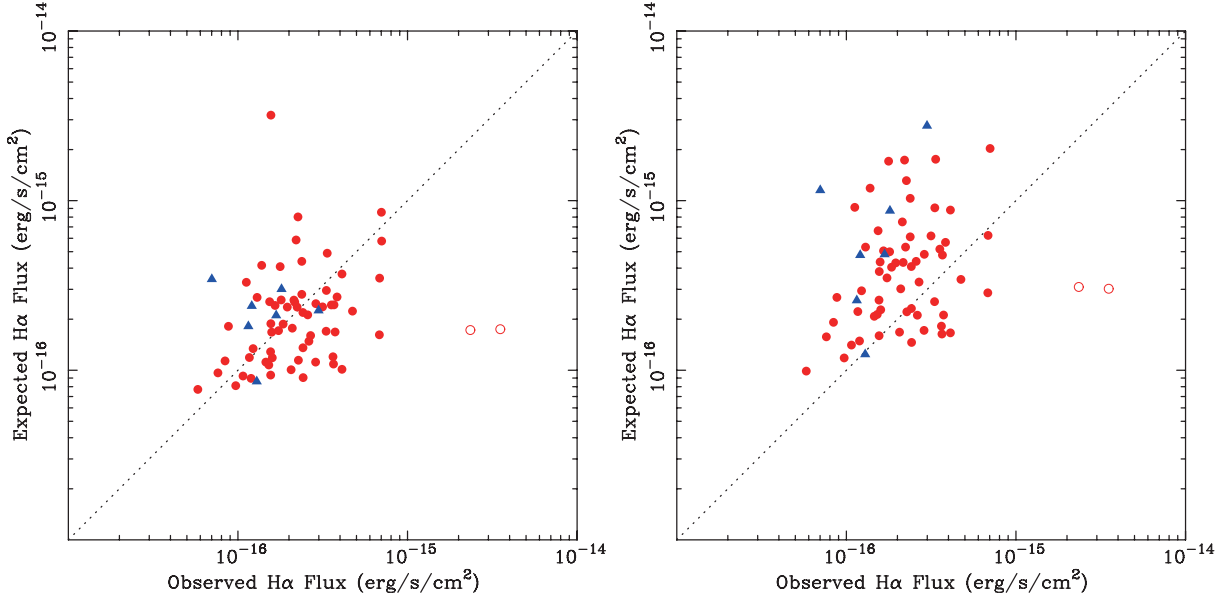


Fig. 6. Comparisons of the observed $H\alpha$ flux and the expected $H\alpha$ flux. The expected $H\alpha$ flux was calculated from the rest-frame UV luminosity corrected by $E(B - V)$ for nebular (left) and stellar (right) components assuming the Calzetti et al. (2000) extinction law. Objects with $> 90\%$ flux loss due to the OH-masks are indicated by red open circles. The AGN candidates in the BPT diagrams are indicated by blue triangles (subsection 3.4).

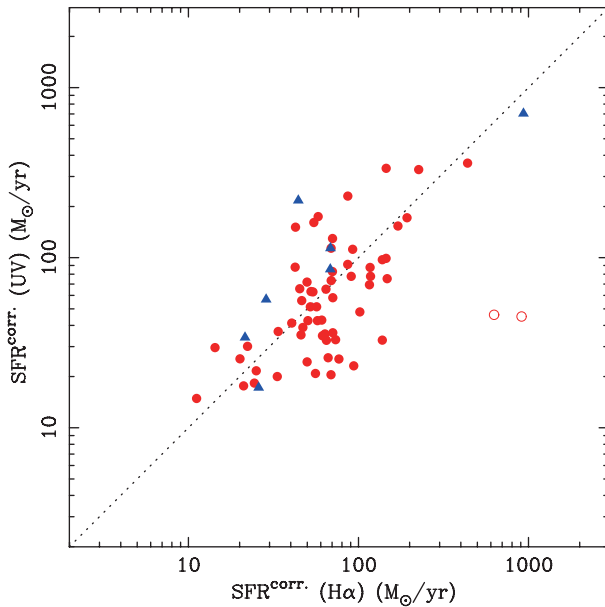


Fig. 7. Comparisons of the extinction corrected SFR obtained from the $H\alpha$ luminosity and that from the rest-frame UV luminosity density. Objects with $> 90\%$ flux loss due to the OH-masks are indicated by red open circles. The AGN candidates in the BPT diagrams are indicated by blue triangles (subsection 3.4).

field (Grogin et al. 2011; Koekemoer et al. 2011). The r_{50} of our primary sample, described in subsection 2.3, in the CANDELS FoV was measured from the F160W (the rest-frame wavelength is slightly different from that in K -band) images deconvolved by a PSF of $0''.18$. We found that they agree well with those derived from the K -band image within $0''.05$ ($\sim 10\%$ accuracy).

The fiber loss for each object was determined from its r_{50} . The seeing size was assumed to be $0''.75$ (FWHM) in the H -band, as expected for the seeing size of $\sim 0''.9$ in the R -band and the wavelength dependence of $\propto \lambda^{-0.2}$ (e.g., Glass 1999). The median r_{50} is $0''.55$ and the corresponding covering fraction is 0.45. Line fluxes that we present in this paper were corrected for this aperture effect.¹ It should be noted that the positional error of the fibre allocation was $\lesssim 0''.2$ (Kimura et al. 2010) and the effect was small ($\lesssim 10\%$). Further, this error was random and did not cause a systematic error.

3.4. Possible AGNs

Detections of $H\alpha$, $[\text{N II}]\lambda 6584$, $[\text{O III}]\lambda 5007$, and $H\beta$ lines allowed us to make a line diagnosis to distinguish AGNs from star-forming (SF) galaxies (Baldwin et al. 1981). $H\alpha$, $[\text{N II}]$, $[\text{O III}]$, and $H\beta$ lines were detected with $S/N > 3$ for 7 objects. $H\alpha$ and $[\text{N II}]$ lines were detected with $S/N > 3$, but both the $[\text{O III}]$ and $H\beta$ lines were not detected for 14 objects. Both the $[\text{O III}]$ and $H\beta$ lines were detected with $S/N > 3$, but the $H\alpha$ and $[\text{N II}]$ lines were not detected for 4 objects. The distribution of these objects on the BPT diagram is presented in figure 8. The empirical criterion to separate the AGN and SF by Kauffmann et al. (2003) and the maximum theoretical line of starburst by Kewley et al. (2001) are plotted. Six objects are in the AGN region if the theoretical line is adopted. In addition to these objects, one object shows a line width larger than 1000 km s^{-1} , suggesting the presence of an AGN. Thus, these seven objects are excluded from the sample hereafter. It is worth stressing that although several objects

¹ Strictly speaking, the aperture loss is already corrected by using the correction factor for a point source in the flux calibration. The correction factor should be different for a galaxy, since it is generally extended. Although we need to modify the correction factor for a galaxy, the modification was less than 10%, and we did not modify it.

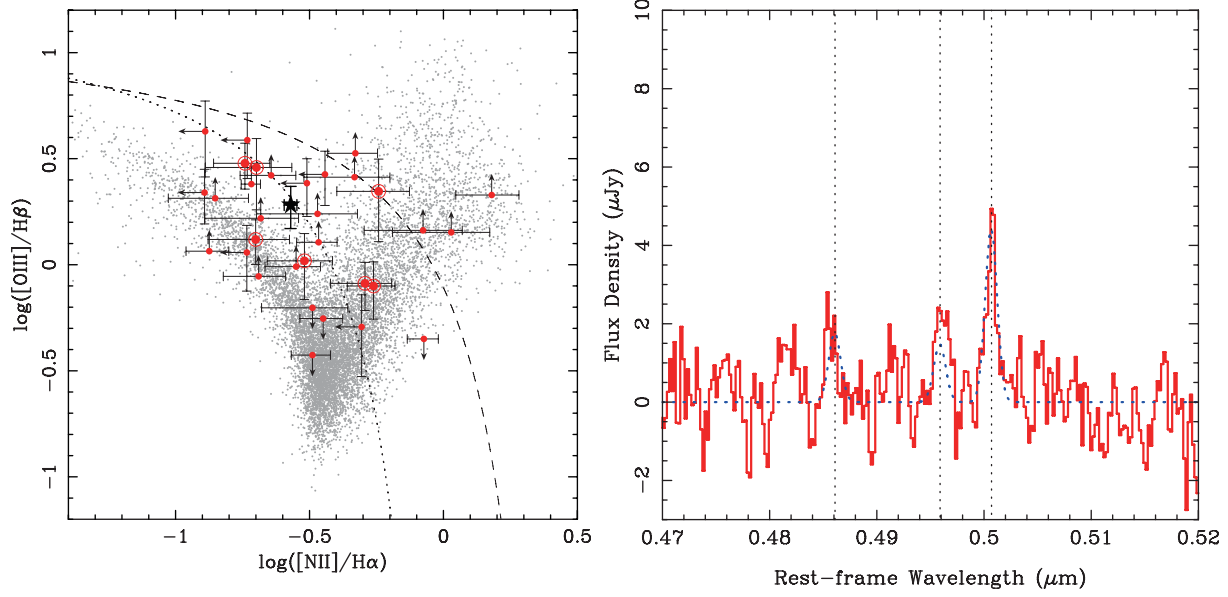


Fig. 8. Left: BPT diagram. Objects with $S/N > 3$ for $H\alpha$, $[NII]$, $[OIII]$, and $H\beta$ are shown by double circles. Upper and lower limits are 3σ values. The result from the stacking analysis is shown by a black star. For a comparison, local SDSS galaxies are plotted as gray dots. The empirical criterion to separate the AGN and SF by Kauffmann et al. (2003) and the maximum theoretical line of starbursts by Kewley et al. (2001) are shown as dotted and dashed curves, respectively. Right: The stacked non-AGN spectrum for the $H\beta$ and $[OIII]$ region.

are located between the theoretical line and the empirical line (often referred to as a *composite* region), most are within the empirical line.

In the right panel of figure 8, we also show the stacked spectrum of all observed spectra, while excluding the seven AGN candidates. The stacking analysis shows that these galaxies at $z \sim 1.4$ are located above the sequence of normal SF galaxies at $z \sim 0.1$. Similar trends have been reported at $z \sim 2$ (Erb et al. 2006; Hainline et al. 2009). By using high S/N spectra of gravitationally lensed galaxies, Hainline et al. (2009) found that the galaxies at $z \sim 2$ show higher $[OIII]/[OII]$ line ratios, and thus higher ionization parameters compared to local SF galaxies. The systematic upward shift of our sample in the BPT diagram also suggests higher ionization parameters in galaxies at $z \sim 1.4$. For this reason, we use the maximum theoretical line by Kewley et al. (2001) as the selection of non-AGNs. However, we cannot completely rule out the possibility of contamination from low-luminosity AGNs.

3.5. Metallicity Determination and Its Uncertainty

Empirical indicators obtained from strong emission lines were used in order to derive the metallicity of high-redshift galaxies. The choice of the indicators depends on the targets' redshift. For galaxies at $1.2 < z < 1.6$, $H\beta$, $[OIII]$, $H\alpha$, and $[NII]$ can be covered in the FMOS wavelength range.

A metallicity indicator with the line ratio of $[NII]$ and $H\alpha$ ($N2$ method) was calibrated by the following equation (Pettini & Pagel 2004):

$$12 + \log(O/H) = 8.90 + 0.57 \times N2, \quad (1)$$

where $N2$ refers to $\log[f([NII]\lambda 6584)/f(H\alpha)]$. The scatter around the relation is ~ 0.18 dex at the 68% significance level (Pettini & Pagel 2004). It is also known

that $[NII]$ tends to be saturated near and above solar metallicity. Pettini and Pagel (2004) found that $O3N2$ ($\equiv \log\{([OIII]\lambda 5007/H\beta)/([NII]\lambda 6584/H\alpha)\}$) is more useful for higher metallicities. For 14 objects in our sample, the $[NII]$, $H\alpha$, $[OIII]$ and $H\beta$ lines are detected with $S/N \geq 2$. For these objects, we compared the metallicity derived by the $N2$ method to that from the $O3N2$ method. We found that the metallicities derived from the $O3N2$ method are systematically lower by 0.07 dex than those from the $N2$ method in the metallicity range of $12 + \log(O/H) = 8.4\text{--}8.8$. The systematic difference of metallicity determination in these two methods by 0.1–0.2 dex was reported at high-redshift (Erb et al. 2006); this may be due to differing physical conditions in SF galaxies at $z \sim 1.4$, as compared to $z \sim 0$.

In figure 5, the metallicity derived from *method1* is compared to that from *method2*. Although the metallicities derived from the two methods generally agree, the scatter is relatively large.

3.6. Stacking Analysis

More than half of the $[NII]$ line fluxes are too weak to measure the $[NII]/H\alpha$ line ratio and thus the metallicity of individual objects reliably. In order to cope with this low significance of the $[NII]$ line and to reveal the 'average' nature of the sample galaxies, we separated the sample into three mass bins, stacked the individual spectra, and derived the metallicity at the representative stellar mass in each bin. We performed the stacking analysis in two ways. One was stacking the best-fit spectra, which were properly corrected for the OH-mask effect, as described above, and the other is simply stacking the observed spectra.

For the former method (stacking the model spectra), each model spectrum was made by a multi-Gaussian profile with

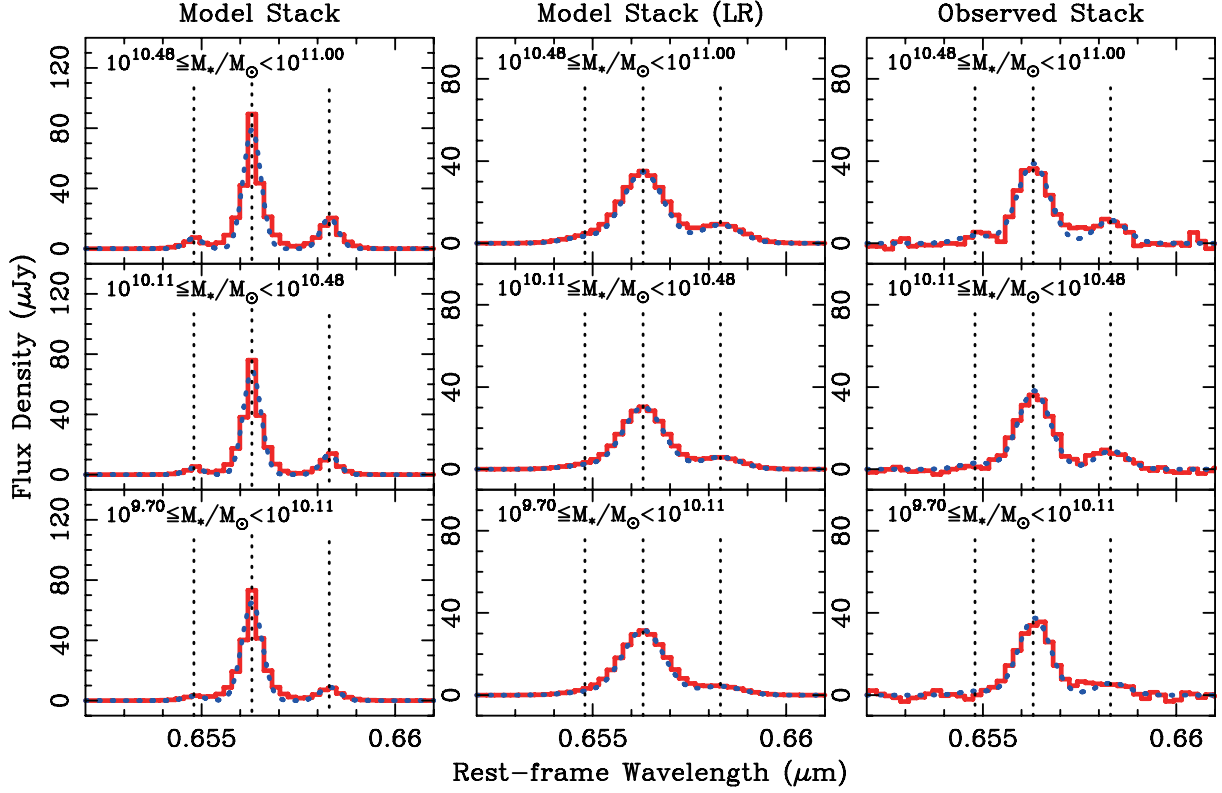


Fig. 9. Stacked spectra in three mass bins (red solid line) and the model fittings (blue dotted line). The profiles from the stacking analysis with best-fit models are in the left panels, those with best-fit models convolved to the LR spectra in the middle, and those with the “observed spectra” in the right panel. The mass ranges (the number of objects in each mass bin) are $10^{10.48} < M_*/M_\odot < 10^{11.00}$ (14), $10^{10.11} < M_*/M_\odot < 10^{10.48}$ (22), and $10^{9.70} < M_*/M_\odot < 10^{10.11}$ (22) from top to bottom. Vertical dotted lines indicate the positions of [N II]λ 6548, Hα, and [N II]λ 6584 from left to right.

the best-fit parameters from *method1* (subsection 3.1). These spectra were combined to give the average spectrum. The obtained spectra were again fitted by multi-Gaussian models to derive the line ratio and the metallicity.

For the latter method (stacking the observed spectra), the observed spectra were averaged with weights based on the observed noise to minimize the effects of the OH-mask, as follows:

$$F_2^{\text{stack}}(\lambda) = \frac{\sum_{i=1}^n \frac{F_i(\lambda)}{\sigma_i(\lambda)^2}}{\sum_{i=1}^n \frac{1}{\sigma_i(\lambda)^2}}, \quad (2)$$

where $F_i(\lambda)$ and $\sigma_i(\lambda)$ are the de-redshifted observed flux density and noise, respectively. The noise is generally large at the OH masks. In the left panel of figure 9, the spectra resulting from stacking the model spectra are shown. In the middle panel, the spectra are convolved to low resolution ($R \sim 800$ at the wavelength). In the right panel, the spectra resulting from stacking the observed spectra are shown. In the low-resolution spectra, the spectra from the two different methods are roughly comparable. In figure 9, it can be seen that the flux of [N II] increases with increasing stellar mass.

The uncertainties associated with the stacking methods were examined by stacking the sample in various ways. For both methods, we examined four different ways of combining the spectra: The weighted average, unweighted average, median,

and flux normalized average. The typical uncertainties are 0.04 dex (the largest mass bin) to 0.07 dex (the smallest mass bin). The uncertainties from the stacking method are almost comparable to or slightly larger than the observational errors.

In the method of stacking the observed spectra, some of the individual emission lines are affected by the OH-masks. This effect is simulated by stacking artificial spectra whose redshift is randomly distributed in the range of $1.2 < z < 1.6$. In this simulation, the line flux of Hα, the ratio of [N II]/Hα, and the line width were assumed to be $1.0 \times 10^{-16} \text{ erg s}^{-1} \text{ cm}^{-2}$, 0.20, and 200 km s^{−1}, respectively, which are typical values for the detected objects. The number of the artificial spectra was ~ 20 , which is comparable to the number of actual objects in each mass bin. We fit the realized spectrum and measured the line ratio and metallicity by *method2*, described in subsection 3.1. This process was repeated 1000 times. The recovered line ratio agrees with the input value within $\sim 20\%$, corresponding to ~ 0.1 dex in metallicity, with no systematic difference.

In this paper, we use the former method, i.e., stacking the model spectra, as a fiducial stacking method. Hereafter, the stacked results are obtained by this method unless otherwise noted.

3.7. The Mass–Metallicity Relation at $z \sim 1.4$

The derived metallicity distribution as a function of stellar mass is presented in figure 10. The stellar masses are

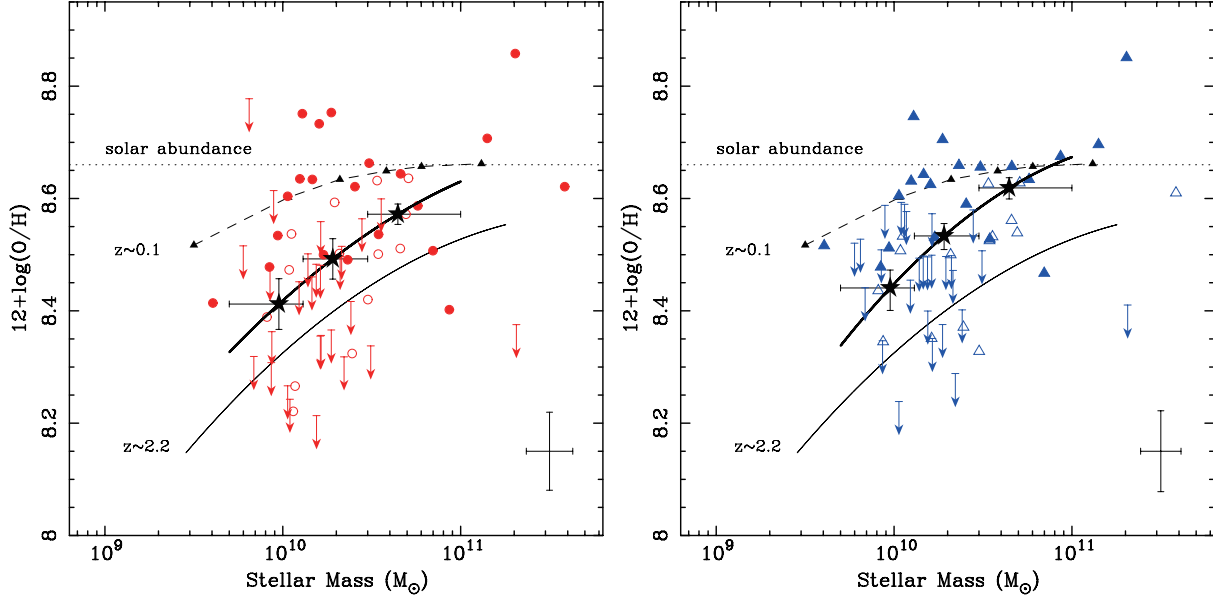


Fig. 10. Metallicity as a function of the stellar mass of our sample. The metallicity derived with spectral fitting with and without the effects of the OH masks are plotted in the left and right panel, respectively. The typical errors of stellar mass and metallicity are shown in the lower right corner of each panel. [N II] lines with $S/N \geq 3.0$ and $1.5 \leq S/N < 3.0$ are indicated by filled and open symbols, respectively. [N II] lines with $S/N < 1.5$ are plotted as upper limits with values corresponding to 1.5σ . Note that the error of the metallicity was derived from the flux error of H α and [N II] lines, and does not include the uncertainty of the metallicity calibration. The results from stacking analysis are presented by filled stars. Thick solid lines are the second-order polynomials for the stacked results. Dashed lines and thin solid lines are the mass–metallicity relation at $z \sim 0.1$ (Tremonti et al. 2004) and $z \sim 2.2$ (Erb et al. 2006). Horizontal dotted line indicates solar metallicity [$12 + \log(\text{O}/\text{H}) = 8.66$; Asplund et al. 2004].

Table 1. Metallicity from the stacked spectra in three stellar mass bins.

$\log(M_*/M_\odot)$	$12 + \log(\text{O}/\text{H})$	
	<i>method1</i>	<i>method2</i>
$9.98^{+0.13}_{-0.28}$	8.412 ± 0.045	$8.441^{+0.032}_{-0.037}$
$10.28^{+0.20}_{-0.17}$	8.492 ± 0.036	$8.530^{+0.022}_{-0.024}$
$10.65^{+0.35}_{-0.17}$	8.572 ± 0.018	$8.619^{+0.018}_{-0.020}$

re-calculated by the SED fitting in the same manner described in subsection 2.2 but fixing the redshift to the spectroscopic redshift obtained by the observations. All other physical quantities are based on spec- z . In the left panel, the metallicities were derived using *method1*, as we describe in subsection 3.6, while in the right panel, we used metallicities derived by *method2*. In both panels, the objects for which the S/N of the [N II] flux is less than 1.5 are plotted as upper limits with values corresponding to 1.5σ . The mass–metallicity relations obtained at $z \sim 0.1$ (Tremonti et al. 2004) and $z \sim 2.2$ (Erb et al. 2006) are plotted for a comparison. Note that the stellar masses from these works are converted by a factor of 1.8, so that the IMF is consistent with that adopted in this paper. The metallicity at $z \sim 2.2$ is obtained by using the same $N2$ indicator, and for that at $z \sim 0.1$ we use the recalculated values with the $N2$ indicator from Erb et al. (2006) for a fair comparison. In both panels of figure 10, typical observational errors of stellar mass and metallicity are shown at the lower-right corner. In these errors, the uncertainty of the metallicity calibration is not included.

Since [N II] emission lines were not detected significantly for $\sim 40\%$ of our sample, we measured the average metallicity by dividing the sample by the stellar mass and applying a stacking analysis including both detections and non-detections in the way presented in subsection 3.6. We divided the sample into three mass bins: $10^{9.70} M_\odot$ – $10^{10.11} M_\odot$, $10^{10.11} M_\odot$ – $10^{10.48} M_\odot$, and $10^{10.48} M_\odot$ – $10^{11.00} M_\odot$. The number of objects in each mass bin is ~ 20 . The metallicities derived from stacked spectra in three stellar mass bins are also presented as solid stars in both panels of figure 10. The errors are estimated by the bootstrap method with 1000 realizations. The resulting mass–metallicity relation obtained by our fiducial method (left panel) is systematically lower by 0.03, 0.04, and 0.05 dex, in the lowest, middle, and highest mass bin, respectively, than that from the observed spectra stacking method. The results are also summarized in table 1.

Figure 10 shows that most individual objects, and the results from the stacking analysis at $z \sim 1.4$ lie between the mass–metallicity relation at $z \sim 0.1$ and $z \sim 2.2$. The stacked results are expressed by a second-order polynomial:

$$12 + \log(\text{O}/\text{H}) = -0.0724x^2 + 1.733x - 1.67, \quad (3)$$

for the model spectra stacking method and

$$12 + \log(\text{O}/\text{H}) = -0.1082x^2 + 2.497x - 5.71, \quad (4)$$

for the observed spectra stacking method, where $x = \log(M_*/M_\odot)$ in both equations. The resulting curves are also presented in both panels of figure 10.

In subsection 3.3, we found that the typical covering fraction of FMOS fiber is ~ 0.5 . The covering fraction by the fibre

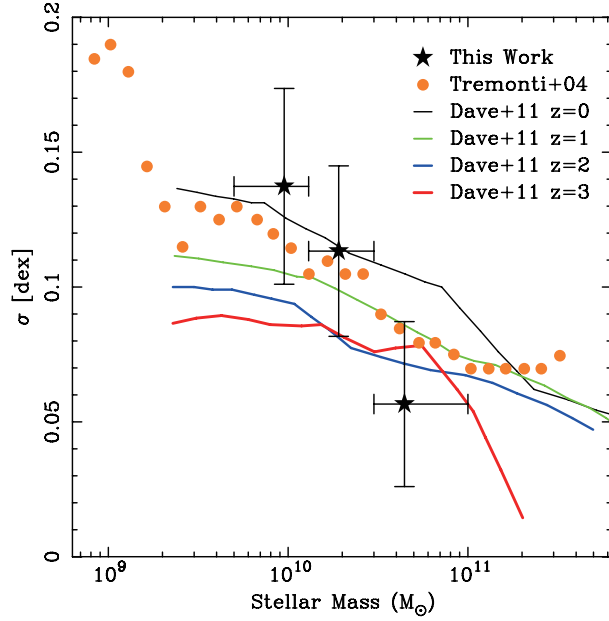


Fig. 11. Intrinsic scatter of the mass–metallicity relation at $z \sim 1.4$ (filled stars). Strictly speaking, this is a lower limit of the scatter. Error bars are based on the bootstrap method. Scatters at $z \sim 0.1$ by Tremonti et al. (2004) are indicated by filled circles and theoretical predictions at $z = 0, 1, 2$, and 3 by Davé, Finlator, and Oppenheimer (2011) are indicated by solid lines.

aperture affects the estimation of metallicity if there is a steep radial metallicity gradient; a small covering fraction leads to an overestimation of the metallicity if the metallicity gradient is negative. Tremonti et al. (2004) showed that the aperture effects on the metallicity is ~ 0.1 dex by using the SDSS galaxies with the typical covering fraction of 0.24. In the local universe, the difference between the metallicity measured in the aperture and the integrated metallicity is $\lesssim 0.1$ dex for the covering fraction of $\gtrsim 0.2$ (Kewley et al. 2005). Since the typical covering fraction of our sample is ~ 0.5 , the metallicity gradient is unlikely to affect the derived metallicity so much unless the metallicity gradient drastically changes at high-redshift. Recently, steeper metallicity gradients than local galaxies have been reported at $z \sim 2$ (Jones et al. 2010; Yuan et al. 2011), while the flatter or even “positive” gradients have also been reported (Cresci et al. 2010). The metallicity gradient at high redshift remains unclear due to the small size of currently available samples.

The intrinsic scatter of the mass–metallicity relation has been reported at $z \sim 0.1$ (Tremonti et al. 2004; Yates et al. 2012), and also reproduced by cosmological simulations (Davé et al. 2011). We try to constrain the scatter of the mass–metallicity relation at $z \sim 1.4$, though the sample size may not yet be large enough. Figure 10 shows that the metallicity distribution has a larger scatter as compared with the typical observational error. So the scatter is defined as the RMS of the deviation from the best-fit mass–metallicity relation [equation (3)] in each mass bin, after subtracting the contribution from the averaged observational error of individual objects. The resulting standard deviations are $\sigma = 0.138, 0.113$, and 0.057 dex in mass bins of $\log(M_*/M_\odot) = 9.98, 10.28, 10.65$,

respectively. Since we take the metallicities from upper limits for many objects, the intrinsic scatter should be larger than these values. Figure 11 shows the intrinsic scatter against the stellar mass. The scatters of the mass–metallicity relation at $z \sim 1.4$ are comparable to those obtained at $z \sim 0.1$ by Tremonti et al. (2004); they decrease with increasing stellar mass of galaxies if we see the face values, though the small scatter at the massive part may be partly due to a saturation effect of the $N2$ indicator.

3.8. Dependence of SFR and Size on the Mass–Metallicity Relation

We examine the dependency of SFR on the mass–metallicity relation for our sample at $z \sim 1.4$. In figure 12, we present the metallicity as a function of the stellar mass for individual objects, dividing into three groups according to their intrinsic SFR s. In the left panel, the SFR is derived from the observed $H\alpha$ luminosity corrected for extinction by using $E(B - V)^{gas}$, described in subsection 2.2, while in the right panel the SFR is derived from the rest-frame UV luminosity density, also corrected for extinction. They show no clear trend that galaxies with higher SFR s show lower metallicities; rather, they show a correlation between the SFR and the stellar mass, i.e., galaxies with larger SFR s have larger stellar masses. In order to test this further, we split the sample in each mass bin into two groups by the median SFR . In each mass bin and SFR group, the best-fit model spectra obtained by *method1* are combined. The results are presented in figure 12 as filled and open stars for higher and lower SFR groups, respectively, as well as in table 2. For both SFR s derived from $H\alpha$ and UV, the resulting metallicities in higher SFR groups are lower than those in lower SFR groups in all mass bins, though the difference at the most massive bin in the right panel is very small. At $M_* = 10^{10} M_\odot$ in the figure 12, the gradient of metallicity against SFR from $H\alpha$ is $\Delta[12 + \log(O/H)]/\Delta[\log(SFR)] \sim -0.6$ dex, which is smaller (steeper) by a factor of ~ 2 than that of ~ -0.3 dex at $z \sim 0.1$ (Mannucci et al. 2010). The metallicity gradient against SFR from UV is ~ -0.4 dex, which is almost similar to that at $z \sim 0.1$.

Figure 13 shows that the dependence of specific SFR , derived from $H\alpha$ (left panel) and the rest-frame UV (right panel), on the mass–metallicity relation is similar to that of the SFR (figure 12), but the trend is relatively unclear. This is probably because the correlation between the stellar mass and the SFR cancels out the dependence on the metallicity.

We also examine the dependency of galaxy size (half light radius; r_{50}) described in subsection 3.3 on the mass–metallicity relation. In figure 14 and table 3, in the same manner as the SFR , we present the metallicity as a function of stellar mass dividing the sample by the size. Both individual and the results from stacking show that galaxies with larger sizes tend to have lower metallicities. In the stacking analysis, the difference is larger as the stellar mass decreases. At $M_* = 10^{10} M_\odot$, the gradient of metallicity with r_{50} is $\Delta[12 + \log(O/H)]/\Delta(r_{50}) \sim -0.1$ dex kpc^{-1} , which is comparable to ~ -0.1 dex kpc^{-1} obtained at $z \sim 0.1$ by Ellison et al. (2008a). Since our survey covers the CANDELS field where deep HST images are available, we can also consider the morphological information for a part of our sample. The number of such galaxies,

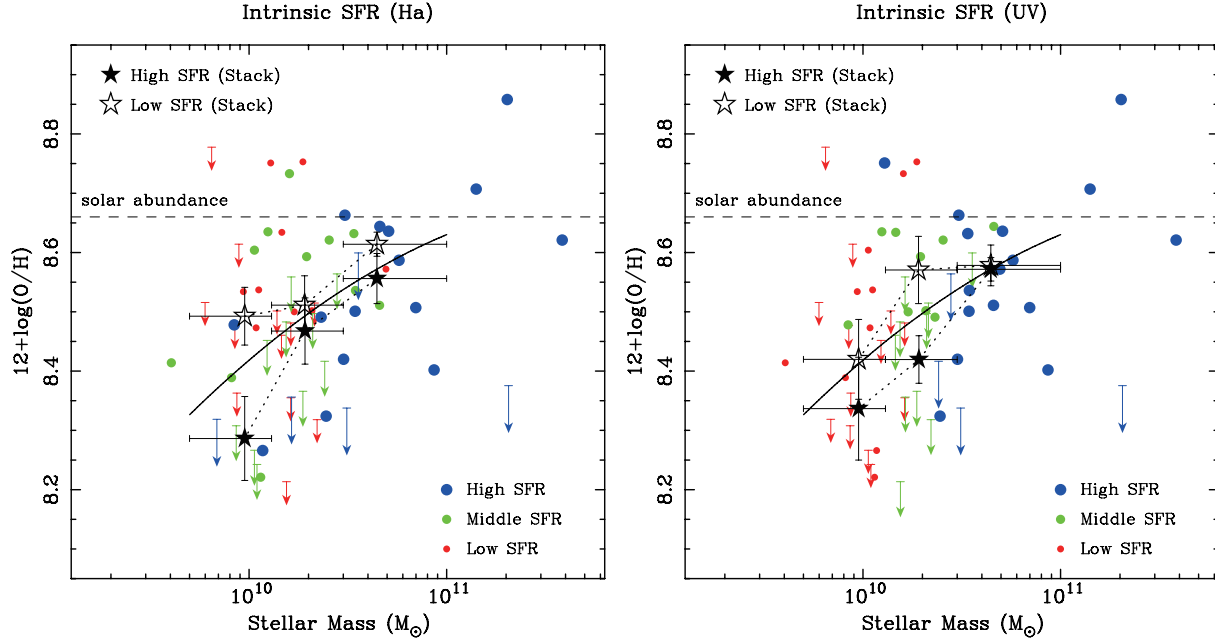


Fig. 12. Dependence of *SFR* on the mass–metallicity relation. In the left panel, the sample is divided into three groups with their *SFR*s derived from $H\alpha$ luminosity corrected for dust extinction: Circles for detection and arrows for non-detection for [N II] with $SFR \leq 53.0 M_{\odot} \text{yr}^{-1}$ (small red), $53.0 M_{\odot} \text{yr}^{-1} < SFR \leq 85.0 M_{\odot} \text{yr}^{-1}$ (middle green), $SFR > 85.0 M_{\odot} \text{yr}^{-1}$ (large blue). In the right panel, the sample is divided by their *SFR*s derived from the rest-frame UV luminosity density corrected for dust extinction, with $SFR \leq 40.0 M_{\odot} \text{yr}^{-1}$ (small red), $40.0 M_{\odot} \text{yr}^{-1} < SFR \leq 80.0 M_{\odot} \text{yr}^{-1}$ (middle green), $SFR > 80.0 M_{\odot} \text{yr}^{-1}$ (large blue). The filled stars show the stacked results in the higher *SFR* group, while the open stars show those in the lower *SFR* group in each mass bin. Solid curves show the mass–metallicity relations described by equation (3) in subsection 3.7.

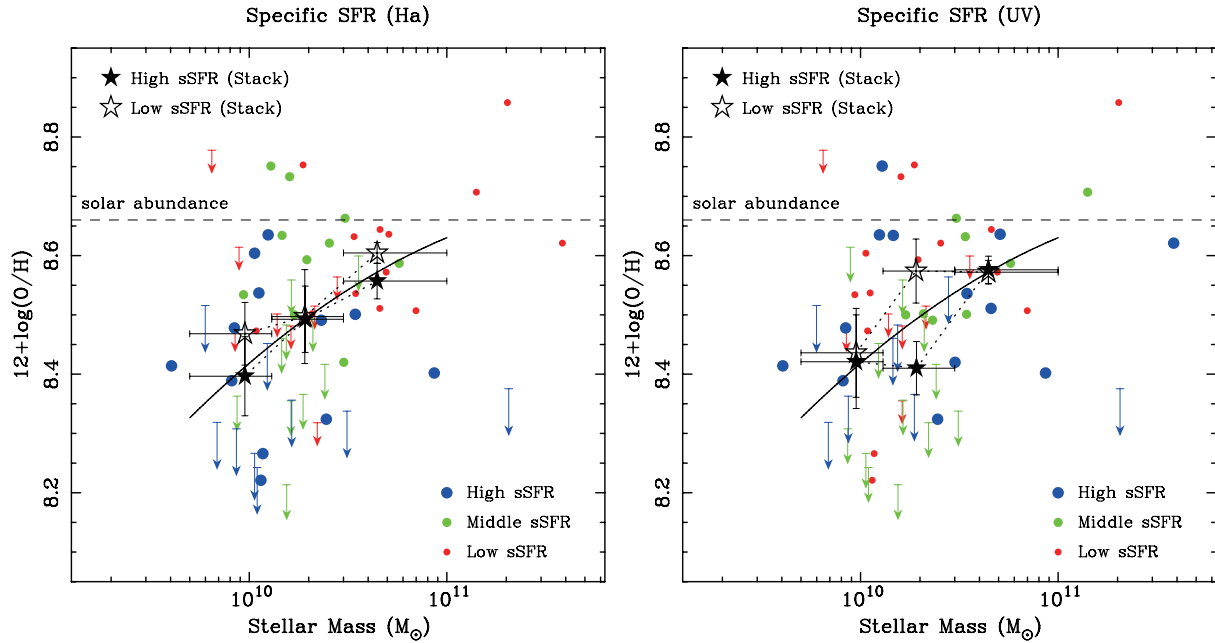
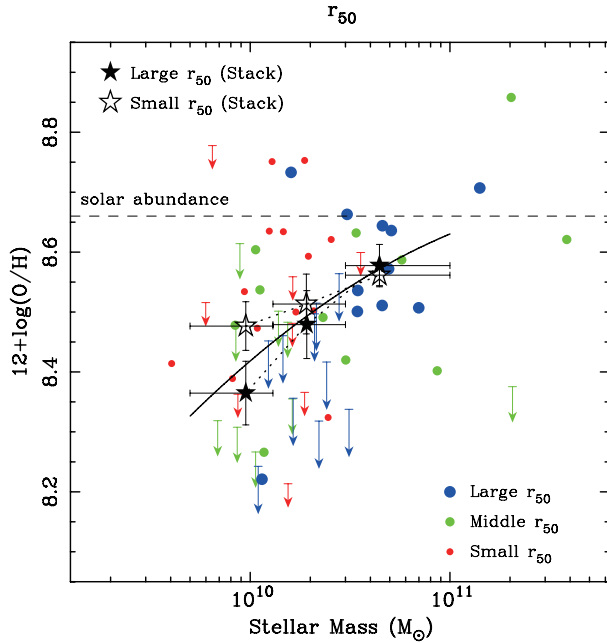


Fig. 13. Dependence of specific *SFR* (*sSFR*) on the mass–metallicity relation. In the left panel, the sample is divided into three groups according to *sSFR*s derived from $H\alpha$ luminosity corrected for dust extinction: Circles for detection and arrows for non-detection for [N II] with $sSFR \leq 2.5 \text{ Gyr}^{-1}$ (small red), $2.5 \text{ Gyr}^{-1} < sSFR \leq 4.0 \text{ Gyr}^{-1}$ (middle green), $sSFR > 4.0 \text{ Gyr}^{-1}$ (large blue). In the right panel, the sample is divided according to *sSFR*s derived from the rest-frame UV luminosity density corrected for dust extinction, with $sSFR \leq 2.3 \text{ Gyr}^{-1}$ (small red), $2.3 \text{ Gyr}^{-1} < sSFR \leq 3.6 \text{ Gyr}^{-1}$ (middle green), $sSFR > 3.6 \text{ Gyr}^{-1}$ (large blue). The filled stars show the stacked results in the larger *sSFR* groups, while the open stars show those in the smaller *sSFR* groups in each mass bin. Solid curves show the mass–metallicity relations described by equation (3) in subsection 3.7.

Table 2. Metallicity from the stacked spectra in three stellar mass bins and two SFR groups.

$\log(M_*/M_\odot)$	$SFR^{\text{med}}(\text{H}\alpha)$ ($M_\odot \text{ yr}^{-1}$)	$SFR^{\text{med}}(\text{UV})$ ($M_\odot \text{ yr}^{-1}$)	$12 + \log(\text{O}/\text{H})$			
			Low SFR (H α)	High SFR (H α)	Low SFR (UV)	High SFR (UV)
$9.98^{+0.13}_{-0.28}$	56.7	25.8	8.493 ± 0.049	8.286 ± 0.071	8.420 ± 0.067	8.337 ± 0.087
$10.28^{+0.20}_{-0.17}$	55.9	54.0	8.511 ± 0.050	8.468 ± 0.056	8.571 ± 0.057	8.420 ± 0.040
$10.65^{+0.35}_{-0.17}$	112.9	91.5	8.614 ± 0.020	8.556 ± 0.042	8.578 ± 0.034	8.572 ± 0.020

**Fig. 14.** Dependence of half light radius (r_{50}) on the mass–metallicity relation. The sample is divided into three groups by their half light radii with $r_{50} < 4.38$ kpc (small red), $4.38 \text{ kpc} < r_{50} < 5.30$ kpc (middle green), $r_{50} > 5.30$ kpc (large blue). The filled stars show the stacked results in the larger SFR (r_{50}) groups, while the open stars show those in the smaller r_{50} groups in each mass bin. Solid curves show the mass–metallicity relations described by equation (3) in subsection 3.7.

however, is too small to be considered statistically. The relation between the metallicity and morphology will be discussed in the future works.

We further examine the dependency of other physical quantities, such as colors, surface mass density, color excess. No clear trend, however, can be seen. It is not certain whether there are truly no trends for such parameters because the sample size is still not large enough. A larger sample from the further survey with FMOS in the future is desirable in order to study these questions.

3.9. Effects of the Sample Selection on the Stellar-Mass Relation

As mentioned in subsection 2.3, our targeted sample is somewhat biased toward the larger SFR end of the galaxy sequence in the M_* – SFR diagram as compared to the primary sample. According to the dependency of SFR on the mass–metallicity relation at $z \sim 1.4$ described above, this selection may lead to a bias toward the smaller metallicity.

Table 3. Metallicity from the stacked spectra in three stellar mass bins and two r_{50} groups.

$\log(M_*/M_\odot)$	r_{50}^{med} (kpc)	$12 + \log(\text{O}/\text{H})$	
		Small r_{50}	Large r_{50}
$9.98^{+0.13}_{-0.28}$	4.4	8.477 ± 0.041	8.365 ± 0.053
$10.28^{+0.20}_{-0.17}$	4.7	8.513 ± 0.050	8.479 ± 0.057
$10.65^{+0.35}_{-0.17}$	5.6	8.562 ± 0.017	8.577 ± 0.035

The expected metallicity of the primary sample at a given stellar mass is examined by assuming the dependency of the SFR on the mass–metallicity relation described in the previous section. The metallicity is expressed as a linear function of intrinsic SFR from UV in each mass bin and expected metallicities of primary sample are estimated from their SFR s. The average metallicity weighted with the H α flux is still close to the metallicity derived in this study within ~ 0.02 dex.

Our sample is also slightly biased toward a larger size as compared with the primary sample. We also examine the effects on the metallicity by assuming the dependency of size on the mass–metallicity relation in the same manner described above. The resulting metallicity is also close to the observed metallicities within ~ 0.03 dex. These effects of both SFR and size on the metallicity are smaller than the other uncertainties. Hence, we conclude that the effects of the selection bias on the mass–metallicity relation are relatively small.

The color excess of our sample distributed widely from 0.0 mag to ~ 0.6 mag with median value of ~ 0.23 mag. The sample is slightly biased toward a smaller color excess as compared with the primary sample (from 0.0 mag to ~ 1.0 mag with the median value is 0.26 mag). However, since there is no clear dependence of color excess on the mass–metallicity relation, the selection effect on the mass–metallicity relation is small.

4. Discussions

4.1. Consecutive Evolution of the Mass–Metallicity Relation from $z \sim 3$ to $z \sim 0$

In figure 15, the mass–metallicity relation obtained in this study is shown with those at $z \sim 0.1$ (Tremonti et al. 2004), at $z \sim 0.8$ (Zahid et al. 2011), at $z \sim 2.2$ (Erb et al. 2006), and at $z \sim 3.1$ (Mannucci et al. 2009). Note again that the stellar mass and the metallicity of these samples are converted so that the IMF and metallicity calibration are consistent with those we adopted. For the conversion of the metallicity, we use

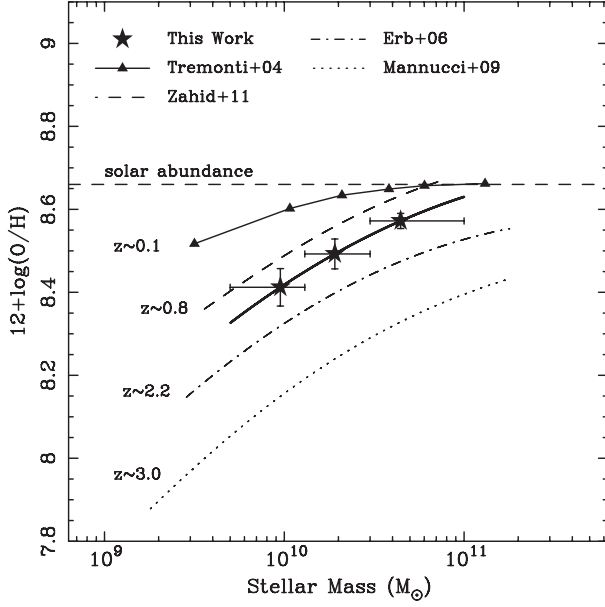


Fig. 15. Comparisons to the mass–metallicity relations at $z \sim 0.1$ (thin solid) by Tremonti et al. (2004), $z \sim 0.8$ (dashed) by Zahid, Kewley, and Bresolin (2011), $z \sim 2.2$ (dotted-dashed) by Erb et al. (2006), and $z \sim 3.1$ (dotted) by Mannucci et al. (2009). The ranges of the relations show the observed range of the stellar masses. The stellar masses and the metallicities of other samples are converted so that the IMF and metallicity calibration are consistent with those we adopted. Horizontal dotted line indicates solar metallicity.

prescriptions by Kewley and Ellison (2008) for the results at $z \sim 0.8$ and by Nagao, Maiolino, and Marconi (2006) for $z \sim 3.1$.

In figure 15, it can be seen that our result at $z \sim 1.4$ is located between that at $z \sim 0.8$ and $z \sim 2.2$ and the mass–metallicity relation evolves consecutively from $z \sim 3$ to $z \sim 0.1$. There appears to be no clear downsizing evolution from $z \sim 3$ to $z \sim 0.8$. It is interesting to note that there seems to be a downsizing-like evolution from $z = 0.8$ – 1.4 to $z \sim 0.1$. The metallicity difference between $z \sim 1.4$ and $z \sim 0.1$ is ~ 0.2 dex at $M_* \sim 10^{10} M_\odot$, ~ 0.1 dex at $M_* \sim 10^{10.5} M_\odot$, and almost comparable at $M_* \sim 10^{11} M_\odot$ if we extrapolate our mass–metallicity relation [equation (3)]. However, here we recall the saturation effect of the N2 indicator. Actually, the recalculated MZ-relation at $M_* \gtrsim 1 \times 10^{11} M_\odot$ for near-solar metallicity. Since the metallicities of our sample at $z \sim 1.4$ are mostly sub-solar, they are not expected to suffer from severe saturation effects. The flat feature at the high mass end at $z \sim 0.1$, however, may be due to the saturation effect.

Since the mass–metallicity relation evolves without changing its shape very much, except for the massive part at $z \sim 0.1$, we trace the chemical evolution at $M_* = 10^{10} M_\odot$. In the upper panel of figure 16, the metallicity at $M_* = 10^{10} M_\odot$ from the mass–metallicity relation at each redshift is plotted as a function of redshift. It clearly shows that the mean metallicity increases with decreasing redshift. The cosmological evolution is well reproduced with $12 + \log(\text{O}/\text{H}) = 8.69 - 0.086(1+z)^{1.3}$. In the lower panel, the metallicity is also plotted against the cosmic age. The metallicity evolution

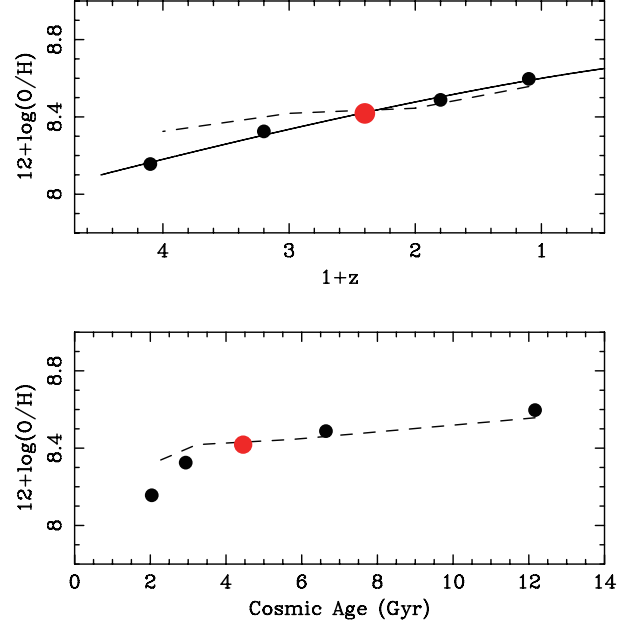


Fig. 16. Evolution of the mean metallicity at $M_* = 10^{10} M_\odot$ against redshift (upper) and cosmic age (lower). The metallicities at $z \sim 0.1$ (Tremonti et al. 2004), $z \sim 0.8$ (Zahid et al. 2011), $z \sim 1.4$ (this work), $z \sim 2.2$ (Erb et al. 2006), and $z \sim 3.1$ (Mannucci et al. 2009) are used. In the upper panel, the linear regression line is also presented as a solid line: $12 + \log(\text{O}/\text{H}) = 8.69 - 0.086(1+z)^{1.3}$. In both panels, the v_{zw} models by Davé, Finlator, and Oppenheimer (2011) are also shown as dashed lines.

rate changes rapidly at $z \gtrsim 2$ and seems to be saturated after that. Interestingly, the end of the rapid growth of metallicity roughly corresponds to the peak epoch of the cosmic star-formation history.

It is worth noting here that the sample selections for these mass–metallicity relations are not necessarily the same. Although the mass–metallicity relation may be affected by the sample selection, pursuing the effect at high redshift is still challenging and will be studied in the future work.

The mass–metallicity relation of our sample is also compared to that obtained from recent cosmological hydrodynamic simulations by Davé, Finlator, and Oppenheimer (2011). They implemented various outflow processes, and found that the momentum-conserving winds, in which both the outflow rate and the wind velocity depend on the velocity dispersion of the galaxy, i.e., galaxy mass, could reproduce the overall shapes of the mass–metallicity relations at $z \sim 0.1$, $z \sim 2$, and $z \sim 3$ well (also shown in figure 16). In figure 17, we show the mass–metallicity relation obtained at $z \sim 1.4$ as well as those in the simulations with four wind models: No winds (*nw*), constant winds (*cw*), slow winds (*sw*), and momentum-conserving winds (*v_{zw}*). We take the average of results at $z \sim 1$ and $z \sim 2$ for comparison at $z \sim 1.4$. Figure 17 shows that our mass–metallicity relation agrees well with the *v_{zw}* model, although it also agrees with the *cw* model within the error bars. This agreement between our mass–metallicity relation and the theoretical *v_{zw}* or *cw* models may possibly indicate the existence of strong and mass-dependent winds in galaxies at $z = 1$ – 2 .

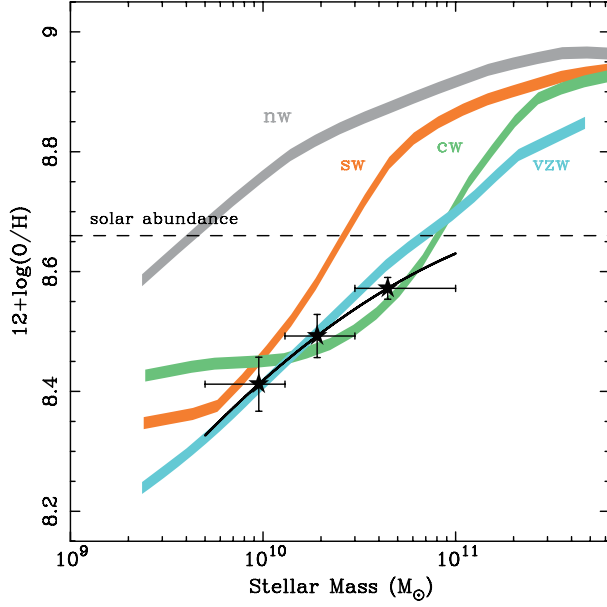


Fig. 17. Comparison to the theoretical models by Davé, Finlator, and Oppenheimer (2011). The theoretical predictions for $z \sim 1.4$ are obtained by averaging those for $z = 1.0$ and $z = 2.0$. No winds (*nw*), Constant winds (*cw*), Slow winds (*sw*), and Momentum-conserving winds (*vzw*) are indicated by gray, green, orange, and cyan, respectively. The observed mass–metallicity relation is the same as that in the left panel of figure 10.

In figure 11, the scatter of the mass–metallicity relation at $z \sim 1.4$ is compared with the predictions at $z = 0$ – 3 with the *vzw* model by Davé, Finlator, and Oppenheimer (2011). While the model shows the evolution of the scatter from $z = 1$ – 2 to $z = 0$, our result shows no clear evolution from $z \sim 1.4$ to $z \sim 0.1$. The estimated scatter in this study, however, is a lower limit. If the scatter at $z \sim 1.4$ is significantly larger than that shown in figure 11, the scatter was larger at the redshift than that seen at $z \sim 0.1$; the scatter of the mass–metallicity relation may decrease as the redshift decreases. This trend is opposite to the simulation by Davé, Finlator, and Oppenheimer (2011). Further deep observations with a larger sample are desirable.

4.2. A Possible Scenario for the Dependence of Various Parameters on the Mass–Metallicity Relation

In subsection 3.8, we presented the dependency of the (specific) *SFR* and galaxy size on the mass–metallicity relation. It is suggested that the *SFR* or specific *SFR* is a second parameter which causes the scatter of the mass–metallicity relation both observationally (Ellison et al. 2008a; Mannucci et al. 2010; Lara-López et al. 2010; Yates et al. 2012) and theoretically (Daé et al. 2011; Yates et al. 2012) at $z \sim 0$. By using SDSS galaxies at $z \sim 0.1$, Mannucci et al. (2010) found that galaxies with larger *SFR* tend to show lower metallicity, and the scatters are significantly reduced by their proposed relation introducing *SFR* as the second parameter, i.e., the fundamental metallicity relation (FMR). They also found that the mass–metallicity relations obtained at $z = 0.5$ – 2.5 are consistent with the FMR at $z \sim 0.1$; the evolution of the mass–metallicity relation from $z \sim 2.5$ to $z \sim 0$ may be explained by the difference

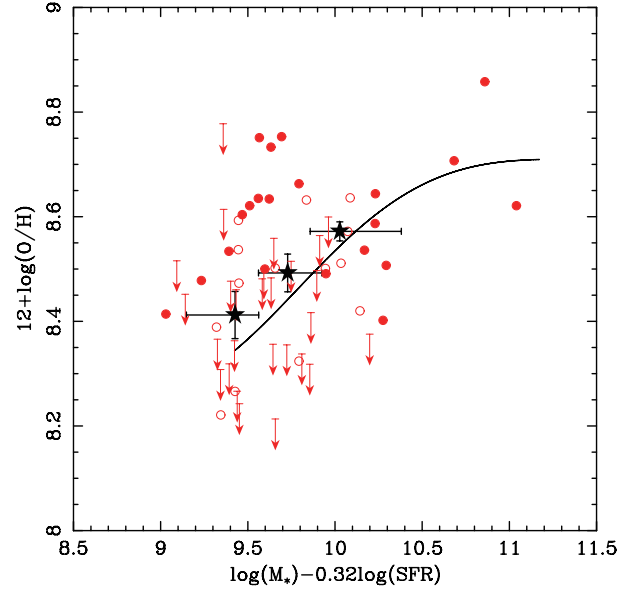


Fig. 18. Metallicity distribution of our sample against $\log(M_*) - 0.32\log(SFR)$, i.e., the fundamental metallicity relation (solid line) proposed by Mannucci et al. (2010). Data points are based on those in the left panel of figure 10.

of *SFR* of the samples. In figure 18, we plot our data points on the fundamental metallicity relation by Mannucci et al. (2010), i.e., metallicity against $\log(M_*) - \mu\log(SFR)$, where μ is a projection parameter. Mannucci et al. (2010) found that $\mu = 0.32$ gives the minimum intrinsic dispersion of metallicity. The metallicity scatter of our sample is not reduced radically by the projection. The average metallicities in all mass bins are close to the FMR, but are shifted slightly; $\mu = 0.22$ gives the best fit. It should be noted, however, that *SFRs* in our sample are mostly larger than those in the FMR at $z \sim 0.1$.

Various interpretations for the large scatter of the mass–metallicity relation and the dependence of second parameters have been discussed. One of the possible interpretation is the dilution effect of infalling gas. The infall of the gas from IGM through cold (smooth) accretion or galaxy mergers is considered to be important in galaxy growth (e.g., Bouché et al. 2010; Hopkins et al. 2006). When pristine gas falls into a galaxy, preexisting enriched gas is diluted by the fresh gas, and at the same time, the new star-formation is likely to occur, raising the *SFR*.

The size dependence can also be explained by the infall of gas. It is suggested that a galaxy merger event can not only supply fresh gas, but also may be able to increase the effective radius of the galaxy (Bezanson et al. 2009; van Dokkum et al. 2010). A correlation between the signal of merger events and the metallicity has been suggested (e.g., Ellison et al. 2008b; Rupke et al. 2010; Sol Alonso et al. 2010). According to their results, interacting or merging galaxies tend to show lower metallicity than isolated galaxies. In our sample, we found that ~ 20 galaxies are closely paired according to a pairing analysis (e.g., Patton et al. 2002) with requirements that (1) the projected separation is < 30 kpc (2) the redshift separation is < 0.15 , which corresponds to 3σ of photo- z uncertainty.

For these objects, however, no clear trends that the interacting galaxies tend to be metal-poor can be found.

5. Conclusions and Summary

We present the first results obtained from near-infrared spectroscopic observations of star-forming galaxies at $z \sim 1.4$ with FMOS on the Subaru Telescope. We observed K -band selected galaxies in the SXDS/UDS fields with $K \leq 23.9$ mag, $1.2 \leq z_{\text{ph}} \leq 1.6$, $M_* \geq 10^{9.5} M_\odot$, and expected $F(\text{H}\alpha) \geq 10^{-16} \text{ erg s}^{-1} \text{ cm}^{-2}$. $\text{H}\alpha$ emission lines of 71 objects were detected significantly. For these objects, excluding possible AGNs identified from the BPT diagram, gas-phase metallicities and upper limits were obtained from $[\text{N II}]/\text{H}\alpha$ line ratio by carefully considering the effects of the OH-masks. We separated the sample into three stellar mass bins, and stacked the spectra. We obtained a mass–metallicity relation at $z \sim 1.4$ from the stacking analysis. The mass–metallicity relation is located between those at $z \sim 0.8$ and $z \sim 2.2$. We tried to constrain an intrinsic scatter of the mass–metallicity relation, and found that the scatter is ~ 0.1 dex, which is comparable to that at $z \sim 0.1$ (Tremonti et al. 2004). The scatter increases as the stellar mass decreases if we take the intrinsic scatters at face-value. The scatters of the mass–metallicity relation at $z \sim 1.4$, however, should be lower limits; this implies that the scatter may be larger at higher redshifts. We found that the deviation from the mass–metallicity relation depends on the SFR and the half light radius: Galaxies with higher SFR and larger half light radii show lower metallicities at a given stellar mass. One possible scenario for the trends is the infall of pristine gas accreted from IGM or through merger events. Our data points show larger scatter than the fundamental metallicity relation (FMR) at $z \sim 0.1$ and the average metallicities

slightly deviate from the FMR. Trends of the dependence of the SFR and the size on the mass–metallicity relation are, however, still not so clear. A larger sample from a further survey with FMOS in the future may be able to reveal clearer trends, not only the dependence of the SFR and the size, but also that of other parameters. The compilation of the mass–metallicity relations at $z \sim 3$ to $z \sim 0.1$ shows that they evolve smoothly from $z \sim 3$ to $z \sim 0$ without changing its shape so much (except for the massive part at $z \sim 0.1$). The metallicity at $M_* = 10^{10} M_\odot$ on the mass–metallicity relation increases with decreasing redshift, and can be described as $12 + \log(\text{O}/\text{H}) = 8.69 - 0.086(1+z)^{1.3}$. The metallicity evolution rate was the highest at the cosmic age of $\lesssim 3$ Gyr, which was before a redshift of 2. However, the result may be influenced by sample selection, and thus further studies with large samples at high redshifts are desirable.

We would like to thank an anonymous referee for useful comments. We are grateful to the FMOS support astronomer Kentaro Aoki for his support during the observations. We also appreciate Soh Ikarashi, Kotaro Kohno, Kenta Matsuoka, and Tohru Nagao sharing fibers in their FMOS observations. KY is financially supported by a Research Fellowship of the Japan Society for the Promotion of Science for Young Scientists. KO's activity is supported by the grant-in-aid for Scientific Research on Priority Areas (19047003). We acknowledge support for the FMOS instrument development from the UK Science and Technology Facilities Council (STFC). DB and ECL acknowledge support from STFC studentships. We would like to express our acknowledgment to the indigenous Hawaiian people for their understanding of the significant role of the summit of Mauna Kea in astronomical research.

References

- Asplund, M., Grevesse, N., Sauval, A. J., Prieto, C. A., & Kiselman, D. 2004, *A&A*, 417, 751
- Baldwin, J. A., Phillips, M. M., & Terlevich, R. 1981, *PASP*, 93, 5
- Bertin, E., & Arnouts, S. 1996, *A&AS*, 117, 393
- Bezanson, R., van Dokkum, P. G., Tal, T., Marchesini, D., Kriek, M., Franx, M., & Coppi, P. 2009, *ApJ*, 697, 1290
- Bolzonella, M., Miralles, J. M., & Pelló, R. 2000, *A&A*, 363, 476
- Bouché, N., et al. 2010, *ApJ*, 718, 1001
- Bouwens, R. J., et al. 2010, *ApJ*, 725, 1587
- Bruzual, G., & Charlot, S. 2003, *MNRAS*, 344, 1000
- Calzetti, D., Armus, L., Bohlin, R. C., Kinney, A. L., Koornneef, J., & Storchi-Bergmann, T. 2000, *ApJ*, 533, 682
- Cid Fernandes, R., Mateus, A., Sodré, L., Stasińska, G., & Gomes, J. M. 2005, *MNRAS*, 358, 363
- Coleman, G. D., Wu, C.-C., & Weedman, D. W. 1980, *ApJS*, 43, 393
- Cresci, G., Mannucci, F., Maiolino, R., Marconi, A., Gnerucci, A., & Magrini, L. 2010, *Nature*, 467, 811
- Daddi, E., et al. 2007, *ApJ*, 670, 156
- Daddi, E., Cimatti, A., Renzini, A., Fontana, A., Mignoli, M., Pozzetti, L., Tozzi, P., & Zamorani, G. 2004, *ApJ*, 617, 746
- Davé, R., Finlator, K., & Oppenheimer, B. D. 2011, *MNRAS*, 416, 1354
- Elbaz, D., et al. 2007, *A&A*, 468, 33
- Ellison, S. L., Patton, D. R., Simard, L., & McConnachie, A. W. 2008a, *ApJ*, 672, L107
- Ellison, S. L., Patton, D. R., Simard, L., & McConnachie, A. W. 2008b, *AJ*, 135, 1877
- Erb, D. K., Shapley, A. E., Pettini, M., Steidel, C. C., Reddy, N. A., & Adelberger, K. L. 2006, *ApJ*, 644, 813
- Furusawa, H., et al. 2008, *ApJS*, 176, 1
- Glass, I. S. 1999, *Handbook of Infrared Astronomy* (Cambridge: Cambridge University Press)
- Grogin, N. A., et al. 2011, *ApJS*, 197, 35
- Hainline, K. N., Shapley, A. E., Kornei, K. A., Pettini, M., Buckley-Geer, E., Allam, S. S., & Tucker, D. L. 2009, *ApJ*, 701, 52
- Hayashi, M., et al. 2009, *ApJ*, 691, 140
- Hopkins, A. M., & Beacom, J. F. 2006, *ApJ*, 651, 142
- Hopkins, P. F., Hernquist, L., Cox, T. J., Matteo, T. D., Robertson, B., & Springel, V. 2006, *ApJS*, 163, 1
- Ilbert, O., et al. 2006, *A&A*, 457, 841
- Iwamuro, F., et al. 2012, *PASJ*, 64, 59
- Jones, T. A., Swinbank, A. M., Ellis, R. S., Richard, J., & Stark, D. P. 2010, *MNRAS*, 404, 1247
- Kajisawa, M., et al. 2011, *PASJ*, 63, S379
- Kauffmann, G., et al. 2003, *MNRAS*, 346, 1055
- Kennicutt, R. C. 1998, *ARA&A*, 36, 189
- Kewley, L. J., Dopita, M. A., Sutherland, R. S., Heisler, C. A., & Trevena, J. 2001, *ApJ*, 556, 121

- Kewley, L. J., & Ellison, S. L. 2008, *ApJ*, 681, 1183
- Kewley, L. J., Jansen, R. A., & Geller, M. J. 2005, *PASP*, 117, 227
- Kimura, M., et al. 2010, *PASJ*, 62, 1135
- Kockemoer, A. M., et al. 2011, *ApJS*, 197, 36
- Lamareille, F., et al. 2009, *A&A*, 495, 53
- Lara-López, M. A., et al. 2010, *A&A*, 521, L53
- Lawrence, A., et al. 2007, *MNRAS*, 379, 1599
- Maiolino, R., et al. 2008, *A&A*, 488, 463
- Mannucci, F., et al. 2009, *MNRAS*, 398, 1915
- Mannucci, F., Cresci, G., Maiolino, R., Marconi, A., & Gnerucci, A. 2010, *MNRAS*, 408, 2115
- Markwardt, C. B. 2009, in *ASP Conf. Ser.*, 411, *Astronomical Data Analysis Software and Systems XVIII*, ed. D. Bohlender et al. (San Francisco: ASP), 251
- Meurer, G. R., Heckman, T. M., & Calzetti, D. 1999, *ApJ*, 521, 64
- Nagao, T., Maiolino, R., & Marconi, A. 2006, *A&A*, 459, 85
- Oke, J. B., & Gunn, J. E. 1983, *ApJ*, 266, 713
- Onodera, M., Arimoto, N., Daddi, E., Renzini, A., Kong, X., Cimatti, A., Broadhurst, T., & Alexander, D. M. 2010, *ApJ*, 715, 285
- Patton, D. R., et al. 2002, *ApJ*, 565, 208
- Pérez-Montero, E., et al. 2009, *A&A*, 495, 73
- Pettini, M., & Pagel, B. E. J. 2004, *MNRAS*, 348, L59
- Rupke, D. S. N., Kewley, L. J., & Barnes, J. E. 2010, *ApJ*, 710, L156
- Salpeter, E. E. 1955, *ApJ*, 121, 161
- Savaglio, S., et al. 2005, *ApJ*, 635, 260
- Sawicki, M. 2011, *ApJS* submitted
- Smail, I., Sharp, R., Swinbank, A. M., Akiyama, M., Ueda, Y., Foucaud, S., Almaini, O., & Croom, S. 2008, *MNRAS*, 389, 407
- Sol Alonso, M., Michel-Dansac, L., & Lambas, D. G. 2010, *A&A*, 514, A57
- Tremonti, C. A., et al. 2004, *ApJ*, 613, 898
- Ueda, Y., et al. 2008, *ApJS*, 179, 124
- van Dokkum, P. G., et al. 2010, *ApJ*, 709, 1018
- Yates, R. M., Kauffmann, G., & Guo, Q. 2012, *MNRAS* in press
- Yoshikawa, T., et al. 2010, *ApJ*, 718, 112
- Yuan, T. T., Kewley, L. J., Swinbank, A. M., Richard, J., & Livermore, R. C. 2011, *ApJ*, 732, L14
- Yuma, S., Ohta, K., Yabe, K., Kajisawa, M., & Ichikawa, T. 2011, *ApJ*, 736, 92
- Zahid, H. J., Kewley, L. J., & Bresolin, F. 2011, *ApJ*, 730, 137